AFOSR-TR- 88-0979

②

DISPERSION STRENGTHENING OF HIGH TEMPERATURE NIOBIUM ALLOYS

Prepared by
D.L. Anton
D.B. Snow
A.F. Giamei

AD-A199 958

ANNUAL REPORT

Contract F49620-86-C-0053

for

Air Force Office of Scientific Research
Building 410
Bolling Air Force Base
Washington, DC 20332

May 31, 1988

DTIC
ELECTE
OCT 0 6 1988
S   D
H

UNITED
TECHNOLOGIES
RESEARCH
CENTER
East Hartford, Connecticut 06108

88 10 5 220

REPORT DOCUMENTATION PAGE

1a. REPORT SECURITY CLASSIFICATION	1b. RESTRICTIVE MARKINGS
Unclassified	

2a. SECURITY CLASSIFICATION AUTHORITY	3. DISTRIBUTION / AVAILABILITY OF REPORT
	unlimited
2b. DECLASSIFICATION / DOWNGRADING SCHEDULE	

4. PERFORMING ORGANIZATION REPORT NUMBER(S)	5. MONITORING ORGANIZATION REPORT NUMBER(S)
R88-917437-2	AFOSR·TR· 88-0979

6a. NAME OF PERFORMING ORGANIZATION	6b. OFFICE SYMBOL (If applicable)	7a. NAME OF MONITORING ORGANIZATION
United Technologies Research Center		AFOSR/NE

6c. ADDRESS (City, State, and ZIP Code)	7b. ADDRESS (City, State, and ZIP Code)
East Hartford, CT 06108	Bld 410 BAFB D.C 20332-6448

8a. NAME OF FUNDING / SPONSORING ORGANIZATION	8b. OFFICE SYMBOL (If applicable)	9. PROCUREMENT INSTRUMENT IDENTIFICATION NUMBER
Air Force Office of Scientific Research	NE	F49620-86C-CCS3

8c. ADDRESS (City, State, and ZIP Code)	10. SOURCE OF FUNDING NUMBERS			
Bolling AFB / Bld 410 Washington, DC 20332-6448	PROGRAM ELEMENT NO.	PROJECT NO.	TASK NO.	WORK UNIT ACCESSION NO.
	61102F	2306	A1	

11. TITLE (Include Security Classification)

DISPERSION STRENGTHENING OF HIGH TEMPERATURE NIOBIUM ALLOYS

12. PERSONAL AUTHOR(S)
D. L. Anton, D. B. Snow, A. F. Giamei

13a. TYPE OF REPORT	13b. TIME COVERED	14. DATE OF REPORT (Year, Month, Day)	15. PAGE COUNT
Annual	FROM 5/87 TO 5/88	1988 May 31	41

16. SUPPLEMENTARY NOTATION

17.	COSATI CODES		18. SUBJECT TERMS (Continue on reverse if necessary and identify by block number)
FIELD	GROUP	SUB-GROUP	Niobium, Creep particle coarsening,
			Dispersion strengthening, Refractory metals.
			High temperature strength

19. ABSTRACT (Continue on reverse if necessary and identify by block number)

Niobium base alloys are very attractive as high temperature materials for advanced gas turbine applications. After many conventional metallurgical approaches, a high temperature creep resistant alloy has yet to be identified which will replace nickel base superalloys. The best chance for obtaining high temperature creep resistance in these alloys is through dispersion strengthening with a stable precipitate that is introduced through rapid solidification. This would result in a very fine dispersion of nonshearable precipitates that would not coarsen upon long term exposure at temperatures in excess of 1200°C.

A study has been conducted here to identify such a stable dispersion, fabricate alloys through a rapid solidification approach and characterize the coarsening of the resulting precipitates. A thermodynamic argument is presented to select candidate dispersions for evaluation. Arc melted and splat quenched alloys were fabricated and evaluated through micro-hardness measurements. An indirect assessment of particle stability is introduced which resulted in a coarsening parameter determined for each candidate precipitate at 1400°C. Microscopic examinations of the more stable alloys were made via optical, extraction and thin foil TEM analyses. Five candidate alloys have been identified for mechanical test evaluation in the third year of this effort.

20. DISTRIBUTION / AVAILABILITY OF ABSTRACT	21. ABSTRACT SECURITY CLASSIFICATION
☐ UNCLASSIFIED/UNLIMITED ☒ SAME AS RPT. ☐ DTIC USERS	Unclassified

22a. NAME OF RESPONSIBLE INDIVIDUAL	22b. TELEPHONE (Include Area Code)	22c. OFFICE SYMBOL
Dr. A. H. Rosenstein	(202) 767-4931	NE

DD FORM 1473, 84 MAR 83 APR edition may be used until exhausted. All other editions are obsolete.

**UNITED
TECHNOLOGIES
RESEARCH
CENTER**

East Hartford, Connecticut 06108

R88-917437-2

Dispersion Strengthening of High
Temperature Niobium Alloys

ANNUAL REPORT

Contract F49620-86-C-0053

APPROVED BY *M. A. de Crescenti*

M. A. DeCrescente, Manager of
Manufacturing Technology and
Process Research

DATE 5/31/88

NO. OF PAGES _____   **COPY NO.** _____

TABLE OF CONTENTS

i

1. INTRODUCTION

The efficiency of current gas turbine engines for aerospace applications is determined by their working gas temperatures. The internal load bearing components are limited in temperature capability by their available strength. The common Ni–base superalloys have a maximum useful temperature of approximately 1176°C (2150°F). In order to obtain improvement in thrust to weight ratio, new materials will need to be developed that are not only strong at high temperatures but also stable in oxidizing environments. These materials must have high strength to density ratios as well. A class of materials which has not been directly utilized in this regard is the refractory metals. In particular, niobium alloys have shown promise as being useful as structural components in high temperature applications due to their relatively low density, stable oxide, low ductile brittle transition temperature and high melting point.

A substantial effort was expended into the possible use of refractory metals as high temperature materials in the 1960's. This effort essentially terminated with the decline of the space program in the United States. However, research has continued in the Soviet Union to the present time. Two basic problems have proved to be difficult to overcome. These are oxidation resistance and high temperature creep strength. The subject of this study is to address the high temperature strength while temporarily disregarding environmental effects. The Soviet literature, as well as conclusions drawn from the western data of the 60's, indicate that for niobium alloys to have useful high temperature strength, strengthening by both solid solution as well as dispersions are necessary.

Reference 1 has dealt with the processing and testing of candidate rapidly solidified Nb alloys containing fine dispersions. A number of alloys were fabricated with the expectation that ZrN, ZrB_2, HfN, or HfB_2 could be introduced as a fine dispersion within a rapidly solidified Nb matrix to impart high temperature creep strength. This effort was met with limited success due to the high reactivity of both Zr and Hf with the ever present oxygen dissolved in the starting Nb metal charge.

After this initial effort, the scope of possible dispersion strengthening precipitates was widened in search of other possible dispersion strengthening candidates. This was accomplished by studying the room temperature hardness of many dispersion strengthened alloys subsequent to high temperature exposure in an attempt to narrow the possible candidate dispersions.

1.1 Stable Dispersion Selection

For a precipitate to be useful as a high temperature dislocation barrier, it must be stable at its use temperature, be of sufficient size so as to present non–shearable obstacles to dislocation motion and be of sufficient volume fraction so as to diminishes Orowan looping. First, for a precipitate to have maximum stability at high temperatures, it must conform to one of the following criteria. It must have low surface energy with the matrix, or have components one of which must have low solubility in the matrix.

Particle coarsening can usually be modeled by the equation:

$$r_o^3 - r^3 = \frac{8V^2 \gamma C_i D}{9RT} t = kt \qquad (1)$$

where r and r_0 are the particle radius at time t and initially, V is the molar volume of the precipitate, γ is the particle/matrix surface energy, C_i is the concentration, D is the diffusion constant of the rate limiting

constituent and k is short–hand notation for the constant term. The interfacial energy, γ, is not expected to vary by more than one order of magnitude as shown in Ref. 2, where a compilation of interfacial energies is given for a number of coherent and incoherent precipitate systems. The molar volume, V, will likewise vary only slightly from one compound to another. Thus the diffusion rate of the dispersion's constituents along with their solubility will be used to determine candidate dispersoids.

The solubility of a dispersion in an alloy matrix will be proportional to its free energy of formation, $-\Delta G$. Low solubility precipitates can be found by limiting our search to very stable particles at temperatures in excess of 1400°C. A reasonably complete listing of free energies of formation for metallurgically important compounds is given in Ref. 4. For a compound to be considered stable in a Nb alloy, it must have a free energy less than its Nb counterpart, in addition to being low in its own right (i.e. < –100 kJ/mole). The free energies for candidate dispersions are given in Table I.

Diffusivities of elements in pure Nb have also been compiled for those experiments using the tracer method in Ref. 3. Table II gives a number of commonly used Nb alloying elements with their frequency factor, D_0, activation energy, Q, and diffusivity at 1400°C. It is interesting to note that at this temperature Ta has a much higher diffusivity than Mo while both C and Y maintain reasonably low diffusivities. It should be remembered that these data are limited to tracer diffusion studies and do not include diffusivity data gained by other means.

In view of the fact that diffusivity data are incomplete, precipitate stability will be judged primarily on free energy arguments. Thus, the selected aim dispersions are given in Table I. One notes that the original aim dispersions of ZrN, ZrB_2 and HfB_2 are on the list and will be pursued further. Data for HfN, the other original dispersion, was not available. In general, the borides look very promising as candidate dispersions as do the silicides; both B and Si have low solubilities in Nb from binary phase diagrams.

The most stable compounds listed here by far are the oxides of Ti, Ta and Y. Oxide dispersion strengthening of Nb alloys has been investigated thoroughly in the past with conclusion that particle coarsening rates were excessively high for their applicability as high temperature dislocation barriers as described previously. The oxides previously examined were those of Zr and Hf while additions of Ti and Ta most assuredly deoxidized the alloys additionally. The free energies of ZrO_2 and HfO_2 are –818 and –828 kJ/mole at 1500°C respectively. These are relatively low free energies (in terms of absolute value) with respect to the borides and nitrides, but the diffusivity of oxygen and the metal atoms supersedes the thermodynamic stability.

Carbides of Zr and Hf have been studied the greatest extent in Nb alloys. The $-\Delta G$ for ZrC at 1500°C is seen to be highest one given in Table I. This gives some indication as to the reason for the carbides' lack of thermal stability.

2. EXPERIMENTAL PROCEDURES

Alloys were fabricated so as to introduce 2 volume percent of the dispersions given in Table I, assuming 100% precipitation, with the inclusion of a pure Nb splat for comparison. Arc melting and splat quenching were performed on these alloys as reported earlier (Ref. 1).

The alloy splats were subsequently cut into sections and wrapped in Nb foil and heat treated in Ti gettered He with an analyzed purity of $< 10^{-7}$ ppm oxygen. Two heat treatment plans were utilized; the first being a solution at 2200°C for 4 hours followed by iterative 1600°C heat treatments for .5, 1, 2, 4, 8 and 16 hours, with the other consisting of a low temperature precipitation of 1200°C for 4 hr with iterative 1400°C heat treatments for the durations stated previously. After each of the iterative heat treatments, one specimen was removed from the furnace and mounted edge on for metallographic and hardness evaluation. Following metallographic preparation, a minimum of five Vickers hardness indents at a 25g load were made to each specimen across their thickness so as to average any chemical gradient or cooling rate effects. The outside edge of the hardness indent was not allowed to come so close to the splat surface as to allow visible buckling and any data points from this near surface region which deviated greatly from the other readings were disregarded and another measurement taken. A typical indent pattern is given in Fig. 1. An optical microscopic examination followed to characterize the grain morphology and any large precipitation which has occurred.

Extraction replicas were taken from splat quenched and aged specimens sectioned edge-on and electropolished in a 12% perchloric acid and methanol solution at −30°C. The replicas were prepared in the standard fashion.

Specimens to be examined by transmission electron microscopy were sectioned with a high speed saw, then ground by hand to a thickness of ≃150 μm and punched into 3 mm discs. These foil blanks were thinned with a South Bay Technology Model 550B jet electropolishing unit with an electrolyte consisting of 500 ml methyl alcohol, 100 ml ethylene glycol monobutyl ether (butyl cellosolve), 90 ml H_2SO_4 (98%), and 30 ml HF (50%). The polishing conditions were 50 VDC, 80 ± 10 mA, and −60 ± 10°C electrolyte temperature. Each side of a disc was polished separately for ≃25 minutes. The thin foils were examined with a Philips EM400T TEM/STEM equipped with an energy–dispersive X-ray spectrometer with light element detection capability.

3. RESULTS AND CONCLUSIONS

3.1 Age Hardening Model

One ca$\pm$correlate hardness data to precipitate size through the following argument. One assumes that hardness, H, is proportional to the yield strength, σ_y (Ref. 5), such that;

$$H \propto \sigma_y \qquad (2)$$

The theoretical correlation between dispersoid particle size and σ_y was developed by Hirsch and Humphreys (Ref. 5) as being;

$$\tau_c = \frac{(0.4Gb)}{\pi \, L} \quad \frac{\ell n(r/b)}{(1-v)^{.5}} \qquad (3)$$

where τ_c is the critical resolved shear stress, L the interparticle spacing which can be further written as $[(\pi/f)^{.5} - 2] \cdot r$ with the precipitate volume fraction volume fraction, f, G the shear modulus, r the particle radius and v Poison's ratio. For our analysis, σ_y can replace τ_c and the following notational simplifications made;

$$B = \ell n(2/b) \qquad (4a)$$

$$A = \frac{(0.4Gb)}{\pi(1-v)^{.5}[(\pi/f)^{.5} - 2]} \qquad (4b)$$

therefore;

$$H \propto Ar^{-1} [B + \ell n(r)] \qquad (5)$$

through diffusion controlled coarsening theory, the precipitate radius can be described as given in eq. 1. By combining eqs. 1 and 5 we obtain;

$$H \propto A \, (r_0 + kt)^{-1/3} [B + \ell n\{(r_0 + kt)^{1/3}\}] \qquad (6)$$

and by neglecting for the moment the hardening of the alloy with particle size and concentrate on the over-aging, the following simplification of eq. 6 can be shown;

$$H \propto AB(r_0 + kt)^{-1/3} \qquad (7)$$

From this point it is clear that for small r_0 (as would be the case in rapidly solidified alloys), by plotting ℓn (H) vs ℓn (t) one should obtain a straight line plot having a $-1/3$ slope. The slope of this line shall be

defined as the unitless softening coefficient, Ψ, and given as:

$$\Psi = -(d\ell n[H]/d\ell n[t]) \tag{8}$$

Two typical isothermal age hardening plots subsequent to the 1200°C precipitation heat treatment are shown in Fig. 2 for the alloys containing ZrC and Ta_5Si_3 respectively. The former shows classical age hardening response with hardening followed by softening due to over-aging. In the latter case only softening was observed, probably due to precipitate growth either during the lower temperature age or because of particle precipitation during rapid solidification.

By plotting these two curves as ℓn (VHN) vs ℓn (t) as described previously, one sees in Fig. 3 that straight line plots are indeed obtained for the age softening portions of the curves. The slopes as determined by a least squares analysis were $\Psi = -0.130$ and -0.065 respectively. While these coarsening coefficients are considerably lower than the -0.333 theoretically expected, this value of Ψ will be used to categorize precipitation phenomena as to their utility at elevated temperature. Close examination of the mathematical argument presented above shows that if an exponential term is present in eq. 2 this would translate to a product of this term times Ψ. The assumptions made above may be in minor error, affecting this term. It will be assumed that if the coarsening exponent is low, that is the alloy over-ages at a slow rate, that the rate limiting step in particle coarsening is slow and the dispersoid may be suitable as a high temperature dispersoid. Conversely, if the material softens rapidly, any dispersoid present acting as a barrier to dislocation motion may be rapidly coarsening, thereby lowering strength.

There are a number of hazards one must guard against in this analysis. For instance, in the event no precipitates are formed, no hardening or softening due to precipitate mechanisms can occur. Thus, the over-aging slope, Ψ, will be nil and one may inadvertently assume a very stable precipitate is present. A measurable coarsening of the particles as monitored through DPH testing will be a prerequisite.

Additionally, some single phase effect will also lead to age softening such as grain growth, oxygen depletion and vacancy annihilation. In order to minimize some of these effects it was found helpful to pre-age the specimens at 1200°C for 4 hours. This brings the rapidly solidified material into a stress relieved state along with precipitating the dispersed phase into a fine yet very small dispersion. To monitor grain growth, which will also be a function of the precipitate process and grain boundary pinning, a pure niobium splat quenched alloy was prepared and aged as noted previously.

3.2 Aging Results

Table III gives the age softening data of the pure Nb and alloyed splat quenched material given the two heat treatments noted in the previous section. In addition to the calculated linear regression data of slope and intercept, the quartile ranking of the 1400°C aged alloys is also given. This ranking will be used to identify candidate dispersions for further microscopic and mechanical test evaluation. Optical examinations were conducted on splat cross sections and the qualitative results are summarized in Table III.

The pure Nb metal is seen to definitely have an age softening character with a unitless softening rate constant of -0.019. Optical metallography reveals that grains grew rapidly upon aging which could be one source of the age softening. In addition it was shown in Ref. 1 that aging in very pure gas results in

deoxidation of the splat material. By lowering the dissolved oxygen concentration the interstitial hardening is diminishing with exposure time. In alloys which tie up the oxygen as oxides, the alloys are to a large extent deoxidized and this effect should be minimized. Considering this as a base line, any alloys with a significantly lower softening rate constant will be considered to have unmeasurable precipitate coarsening by this technique.

The 1600°C aged alloys displayed either very low or very high age softening rates. The very low softening rate constants, ± 0.005, which are seen in the carbide containing alloys are indicative of minimal over-aging due to either totally over-aged precipitates or possibly solutioned precipitates. This is consistent with previous findings that carbides are not significant dislocation barriers at high temperatures. The high softening rate constants of 0.156 and 0.050 were observed in nitride containing alloys, while the boride containing alloys maintained moderate rate constants of ± 0.030. Additionally, all of the grain structures after this heat treatment were equiaxed, indicating that extensive grain growth has occurred. The borides and nitrides still display properties which make them desirable as high temperature dislocation barriers.

The 1600°C exposure has proved to be too severe. Possible candidate precipitates either coarsen too rapidly, are over-aged during the 2000°C "solutioning" treatment or go into solution. Thus a lower heat treatment was devised. An age at 1200°C is expected to precipitate particles from the rapidly quenched metastable solid solution into a fine evenly distributed dispersion. Further aging at 1400°C will serve as the test temperature.

The softening rate constants at 1400°C varied from 0.014 for SiO_2 as a possible precipitate to 0.131 for ZrC. This was considered an ideal distribution from which candidate dispersions could be selected. These dispersions were ranked into quartiles according to softening rate. Two alloy additions, Y and Ti/N, displayed a typical behavior and could not be readily ranked and were put into the fourth quartile. These alloys will be briefly discussed later.

The alloys with the greatest softening rate constants, in the third quartile, contained carbides of Hf and Zr, the carbide resulting from the commercial alloy containing Ta, Zr and C and the nitrogen only alloy. It was not surprising to find the carbides in this quartile since their high temperature stability is known to be insufficient. Additionally, the free energy, $-\Delta G$, of ZrC is the highest of those tested here (see Table I), giving experimental validation to the precipitate stability argument set forth previously.

The age hardening curves of this group are typified by Figs. 2 and 3, with rapid hardening followed by softening over an extended time. The grain structure as observed optically after an 8 hour exposure at 1400°C is equiaxed, further evidence of over-aged precipitates which did not pin the grain boundaries. An optical micrograph of one such alloy is given in Fig. 4 where the equiaxed grain structure is evident. In addition, many relatively small dispersoids can also be identified distributed throughout the matrix. However, any precipitates which can be optically identified are too large to be effective as a dislocation barriers.

Those alloys composing the second quartile contained ZrB_2, HfN, and Si_3N_4. The two former alloys were originally proposed and are still under consideration while the latter dispersion was chosen based on the free energy arguments. Their softening coefficients, Ψ, ranged from 0.023 to 0.032 and the microstructure revealed columnar grain structure. This grain structure, remnant from the rapidly solidified

state indicates grain boundary pinning by a dispersion. Indeed, grain boundary precipitates were observed for all of the alloys in this quartile and a representative micrograph is given in Fig. 5 from the Hf–N containing alloy. Figure 6a illustrates a typical age hardening curve of this group. Hardening occurred totally within the first half hour of aging at 1400°C with age softening resulting after further aging. The extended softening allowed good fitting of the data to the ℓn–ℓn model proposed. This fit is shown in Fig. 6b.

Those alloy compositions which fell into the first quartile were not as uniform as those in the preceding two groups. One hardening curve given in Fig. 7, for the Ti–B alloy, shows initial age hardening through two hours followed by softening with a slight hardness increase after 16 hours at temperature. The same response was obtained for both the Ti and Si containing alloys. Since both Ti and Si are very strong oxide formers, the inadvertant introduction of oxygen during the aging treatment may have caused further precipitation, beyond what was present upon rapid solidification. These three alloys were not heat treated simultaneously, and they were aged with other alloys which did not display this hardening at 16 hours. This eliminates the possibility of oxygen contamination during one heat treatment. The slight secondary hardening at 16 hours, the only data point for which this was observed, moderated the softening parameter in the regression analysis.

As shown in Table III, two of these alloys contained equiaxed grain structures with the Si containing alloy retaining the columnar grain structure and fine dispersions. Very large precipitates were observed in the Ti–B containing alloy but were not identified.

Those alloys ranked in the fourth quartile did not show classical age hardening response and little change in hardness above experimental error could be identified. The Ti–N containing alloy was much different than the other alloys in that a large hardness increase upon aging at 1400°C for 0.5 hours occurred, see Fig. 8. The hardness varied about the mean of approximately 275 by ± 10 through the 16 hours of aging. Extensive electron microscopy will be shown of this system in the following section, but it is expected that a short range ordering reaction is occurring on cooling from 1400°C which results in the high hardness at ambient temperatures.

The softening coefficients, Ψ, can be plotted as a function of free energy, $-\Delta G$, which is given in Fig. 9. The borides and Si_3N_4 are clustered together at low softening coefficients and having $-\Delta G$'s between 200 and 400 kJ/mole. The remaining alloys display a broad trend of decreasing softening coefficient with increasing $-\Delta G$, as would be predicted from the free energy arguments proposed. The aforementioned cluster of relatively low free energy compounds may be due to low diffusivities of the constituents.

3.3 Extraction Replicas

In order to identify some of the precipitates noted in Table III in the aged alloys from the first and second quartile ranking, extraction replicas were cast of the splat quenched and specimens after aging at 1400°C for 8 hours. From the second quartile rank, both the Zr–B and Hf–N aged containing alloys clearly showed a fine dispersed phase within the grains in addition to somewhat larger grain boundary precipitates. In the case of the Zr–B alloy, Fig. 10, the grain boundary phases were identified as rich in Zr and O while the blade like phase within the grains was rich in only Zr. The detector used was not sensitive to boron, and it is suspected that these were ZrB_2 precipitates from this analysis.

The Hf–N containing alloy shown in Fig. 11 has many inter– and intra–granular precipitates which were identified as Hf and oxygen rich with no evidence of N in the alloy (see Fig. 11b). Not shown in this micrograph were some very large globular particles identified as a Hf and Nb rich. There are no known intermetallics in the Hf–Nb system and the identity of these particles is unknown at this time.

Figure 12 illustrates the microstructure of the Si–N containing alloy. No particles were extracted after electropolishing, but a plate–like phase shown in this figure was prevalent. Silicon has limited solubility in Nb from the phase diagram (Ref. 2). Characterization of these platelets will be identified in a later report. They are however quite large, up to 9μm in diameter, and unevenly spaced.

The specimens from the first quartile ranked alloys generally did not yield high quality replicas due to a featureless surface. Particles were, however, identified through EDS analysis. The Si alloy contained a grain boundary phase rich in both Si and Nb with little interstitial element concentration, Fig. 13a. A finely dispersed plate–like phase was shown to be rich in Nb and nitrogen, oxygen and carbon, Fig. 13b. The extent of this precipitate is unknown because of the poor replica quality, but since none of these elements was intentionally added, it is expected that these are only minor constituent phases.

3.4 Thin Foil Microscopy

3.4.1 Nb–8.3Mo–0.05Ti–0.48NbB (nominal wt) ≈ Nb–8Mo–0.1Ti–0.1B (at%)

The lattice parameter of the BCC matrix of splat quenched Nb–8.3Mo–0.05Ti–0.48NbB was determined from [001] selected area diffraction patterns (SADP's), using a thin foil specimen with a layer of gold sputtered onto its surface. This procedure yielded a lattice parameter of $3.295\pm.015$ Å, which suggested that less than 8 at% Mo was present in solid solution after arc melting. Knowledge of this a_0 made it possible to calibrate the camera constant of subsequent individual SADP's by using the matrix spot spacings.

Examination of the microstructure of Nb–8.3Mo–0.05Ti–0.48NbB in the as–splat–quenched condition revealed a strikingly geometric array of thin intragranular precipitates (Figs. 14–16). Figs. 14 and 15 are two–beam bright field images, $\bar{g} = [110]$ in the former case, and $\bar{g} = [002]$ in the latter. The direction of view is close to [100]. Most of the precipitates in dark contrast are thin plates of orthorhombic NbB; a_0 = 0.3292 nm, b_0 = 0.8713 nm, c_0 = 0.3165 nm (Ref. 8). Both the diffraction patterns (Figs. 16–17) and the observed orientations (Figs. 14–15) of the NbB indicated that three variants had precipitated, each with [010] NbB || {100} matrix.

Aging at 1200 or 1400°C resulted in the complete dissolution of the NbB precipitates observed in the splat quenched specimens.

3.4.2 Nb–1.2Ti–0.6N (nominal at%)

As–splat–quenched specimens of this alloy were supersaturated; no precipitates were observed in the thin foil specimens. Specimens aged at 1200°C for 4 hours contained several types of precipitates; ranging from dark, blocky particles at both intergranular and intragranular sites, to thin rods with approximate diameters of 30 – 60 nm and lengths of 30 – 100 nm (Fig. 18).

The grain boundary precipitates (Fig. 19) were identified by selected area (Fig. 20) and convergent beam diffraction (CBED) to be hexagonal Nb_2N (Table IV). In a few instances, the Nb_2N precipitates had coalesced along grain boundaries to form a continuous row (Figs. 21-22), but this was not commonly observed. The presence of kinematically forbidden 0001 reflections in the $< 11\bar{2}0 >$ CBED's (Fig. 22) is not unusual in compounds of this type (e.g. Cr_2N and $A\ell N$ Ref. 10).

The larger, dark intragranular precipitates shown in Figs. 18 and 23 were identified by selected area diffraction as the same phase which was observed at the grain boundaries: hexagonal Nb_2N. The short rows of multiple spots centered on each Nb_2N spot which are visible in Fig. 23C suggest the presence of stacking faults, or possibly twins.

The small, rod shaped precipitates which were randomly distributed throughout the grains (Fig. 18) were identified by crystallographic data, first by using convergent beam diffraction to tilt the thin foil near a major precipitate zone axis, then by evaluating SADP's to obtain quantitative lattice plane spacing data (Fig. 24, Table V). The relative orientations of the superimposed matrix and precipitate patterns suggests the following crystallographic relationship; $\{\bar{1}12\}$ TiN $||$ $\{\bar{1}12\}$ Nb matrix and $< \bar{1}1\bar{1} >$ TiN $||$ <110> Nb matrix.

4. CONCLUSIONS

From the efforts expended in the second year of this study, a methodology was presented to select candidate dispersoids from which high temperature creep resistant mircostructures will be chosen. This methodology is based on classical solute diffusion limited coarsening theory. A model was proposed to quantify rapidly the coarsening of dispersion strengthened alloys by means of micro–hardness measurements applied to isothermally aged rapidly solidified specimens. The model worked well, identifying candidate precipitation strengthened alloys which displayed minimal age softening as quantified by the unitless age softening coefficient, $\Psi = -(d \, \ell n[H]/d \, \ell n[t])$. A correlation between Ψ and the free energy of formation, $-\Delta G$, was observed to hold for some of the alloys, but broke down for some of the more promising candidates in which a lower Ψ value was measured than could be predicted from the empirical correlation. The most promising dispersoid candidates thus far identified are ZrB_2, HfN and Si_3N_4. Full evaluation of ZrN and HfB_2, the remaining two candidates originally proposed, have not been completed. Aging at 1600°C resulted in rapid over–aging of all the alloys evaluated thus far. This indicates an upper bound in temperature which can be expected from these dispersions as being between 1400 and 1600°C.

REFERENCES

1. D. L. Anton, A. F. Giamei And D. B. Snow, Dispersion Strengthening Of High Temperature Nb Alloys, AFOSR Rpt. F49620–86–C–0053, 1987.

2. J. W. Martin and R. D. Doherty, Stability of Microstructures in Metallic Systems, Cambridge University Press, Cambridge, G. B., 1976.

3. J. Askill, Tracer Diffusion Data for Metals and Simple Oxides, Plenum Press, New York, NY, 1970.

4. E. A. Brandes, Smithells Metals Reference Book, 6th ed., Butterworth & Co., London, G. B., 1983.

5. J. B. Cahoon, W. H. Broughton and A. R. Kutzak, Metall. Tans., 2, 1979, (1971).

6. I. M. Lifshitz and V. V. Slyozov, J. Phys. Chem. Sol., 19, 35, (1961).

7. C. Wagner, Z. elektrochem., 65, 581, (1961).

8. M. Hansen: Constitution of Binary Alloys, Second Edition, 1958, McGraw–Hill, New York, p. 255.

9. R. P. Elliott: Constitution of Binary Alloys, First Supplement, 1965, McGraw–Hill, New York, p. 191.

10. J. Mansfield: Convergent Beam Electron Diffraction of Alloy Phases, 1984, Adam hilger, Bristol, pp. 63, 87.

11. F. A. Shunk: Constitution of Binary Alloys, Second Supplement, 1969, McGraw–Hill, New York, p. 533.

Table I

Free Energies of Formation for Candidate Dispersions

Compound	$-\Delta G_{1500}$ (kJ/mole)
<u>NbN</u>	•••
Si_3N_4	251
TiN	195
ZrN	223
<u>NbB$_2$</u>	235
CeB_6	313
HfB_2	316
TiB_2	303
ZrB_2	302
<u>Nb$_2$C</u>	•••
ZrC	184
<u>NbSi$_2$</u>	131
Ta_5Si_3	361
Mo_5Si_3	323
<u>NbO$_2$</u>	518
Ta_2O_5	1413
Ti_3O_5	1797
Y_2O_5	1482

Table II

Tracer Diffusion Data in Pure Niobium

Element	D_0 (cm²/sec)	Q (kcal/mole)	$D_{1500°C}$ (cm²/sec)
Ti	0.40	88.5	0.039
Zr	0.47	87.0	0.460
Ta	1.00	99.3	0.970
Y	1.5×10^{-3}	55.6	0.001
C	3.3×10^{-2}	37.9	0.033

Table III

Candidate Dispersoids and Age Hardening Results

Alloy Number	Alloy Composition	Aim Ppt.	$\frac{-d\,\ell n(H)}{d\,\ell n(t)}$	Quartile	Int.	Aging Temperature	Grain Morphology	Precipitation
	Pure Nb	—	0.019		2.081	1400	Equiaxed	None
H87–12A	Mo–Zr–N	ZrN	0.156		2.530	1600	Columnar	None
–12B	Zr–N	ZrN	0.050		2.072	1600	Equiaxed	Very Large
			0.057		2.143			
–12C	Zr–B	ZrB$_2$	0.012		2.348	1600	Equiaxed	Prior G. B. Ppt.
–12D	Hf–B	HfB$_2$	0.030		2.161	1600	Equiaxed	Very Large
–24A	Zr–C	ZrC	0.004		2.123	1600	Bamboo	Acicular Ppt.
–24B	Hf–C	HfC	0.005		2.085	1600	Equiaxed	G. B. Ppt.
–12C	Zr–B	ZrB$_2$	0.027	2	2.323	1400	Columnar	G. B. Ppt.
–22A	Mo–Ta–Zr–C	ZrC	0.034	3	2.465	1400	Columnar	
–13A	Hf–N	HfN	0.023	2	2.354	1400	Columnar	G. B. Ppt.
–23B	Ta–Si	Ta$_5$Si$_3$	0.065	3	2.313	1400	Columnar+Equiaxed	
–24A	Zr–C	ZrC	0.131	3	2.208	1400	Equiaxed	"mottled"
–24B	Hf–C	HfC	0.039	3	2.075	1400	Equiaxed	"mottled"
–24C	Ti–B	TiB$_2$	0.019	1	2.196	1400	Equiaxed	Very Large
–25A	Ti	Ti$_2$O$_3$	0.022	1	2.389	1400	Equiaxed	
–25B	Si	SiO$_2$	0.014	1	2.386	1400	Columnar	Small Ppt.
–25C	N	NbN	0.097	3	2.372	1400	Columnar	Small Ppt.
H88–06	Si–N	Si$_3$N$_4$	0.032	2	2.500	1400	Columnar	G. B. Ppt.
–08	Ti–N	TiN	—	4	—	1400	Columnar	Small Ppt.
–09	Y	Y$_2$O$_3$	—	4	—	1400	Columnar	Small Ppt.

Table IV

Observed vs. Calculated Lattice Parameters, Nb_2N Precipitates
$< 11\bar{2}0 >$ Zone Axis Patterns

Observed d's (nm)

Plane	Fig. 20	Fig. 23	Calculated[*] d's (nm)
(0001)	0.500	0.495	0.496
($1\bar{1}00$)	0.267	0.264	0.265
($1\bar{1}01$)	0.236	0.233	0.234
($1\bar{1}02$)	0.182		0.181

[*] $a_0 = 0.3058$ nm; $c_0 = 0.4961$ nm (Ref. 9)

Table V

Observed vs. Calculated Lattice Parameters, TiN Precipitates
$< 11\bar{2} >$ Zone Axis Patterns

Plane	Observed d's (nm) Fig. 24	Calculated* d's (nm)
(111)	0.244	0.244
($2\bar{2}0$)	0.149	0.149
($3\bar{1}1$)	0.126	0.126

* a_0 = 0.4224 nm (Ref. 11)

50 μm

Figure 1.   Typical Vickers Hardness Indent Pattern in Alloy H87-12C After 1 hr
Age at 1600°C
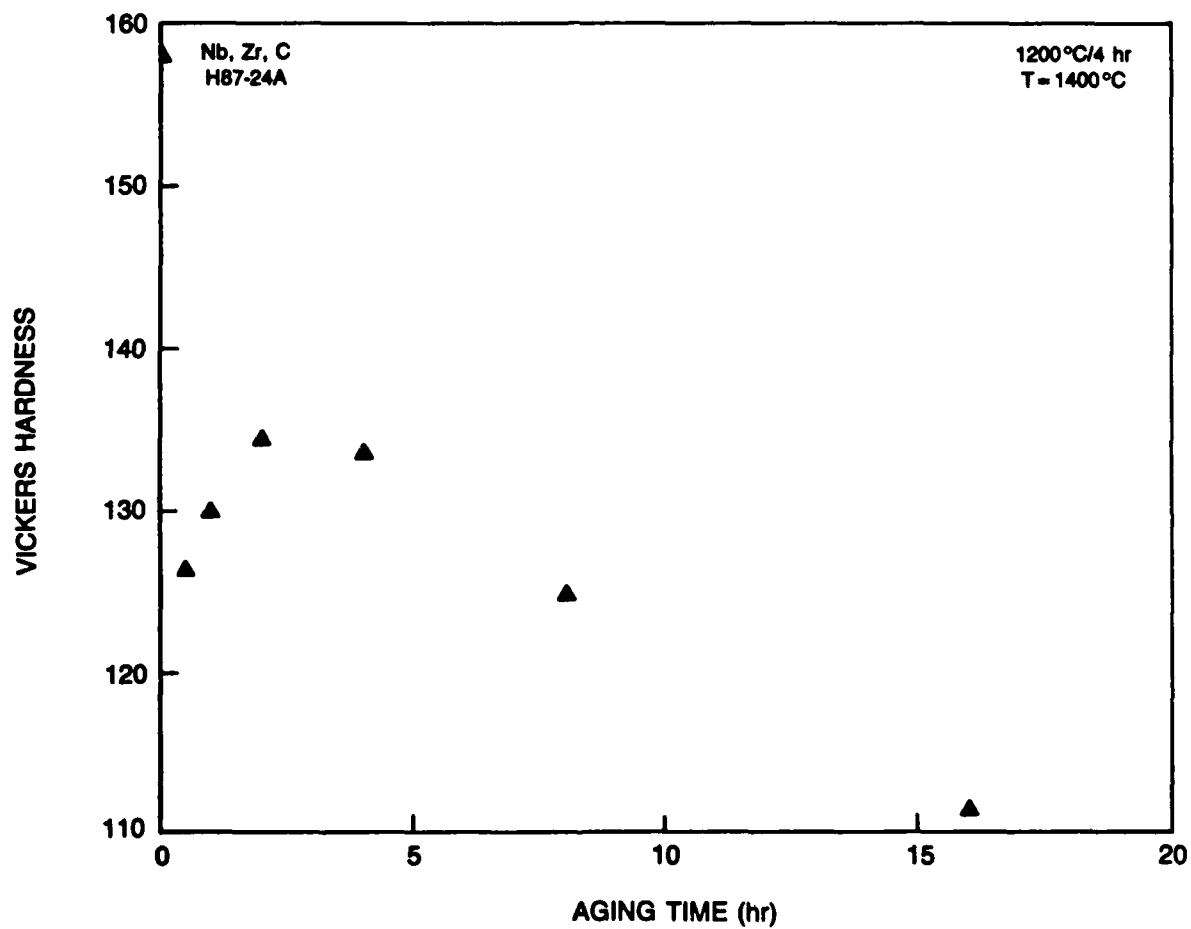
Figure 2.   Isothermal Age Hardening Plot for ZrC Hardened System Showing Classical Age Hardening Followed by Softening.
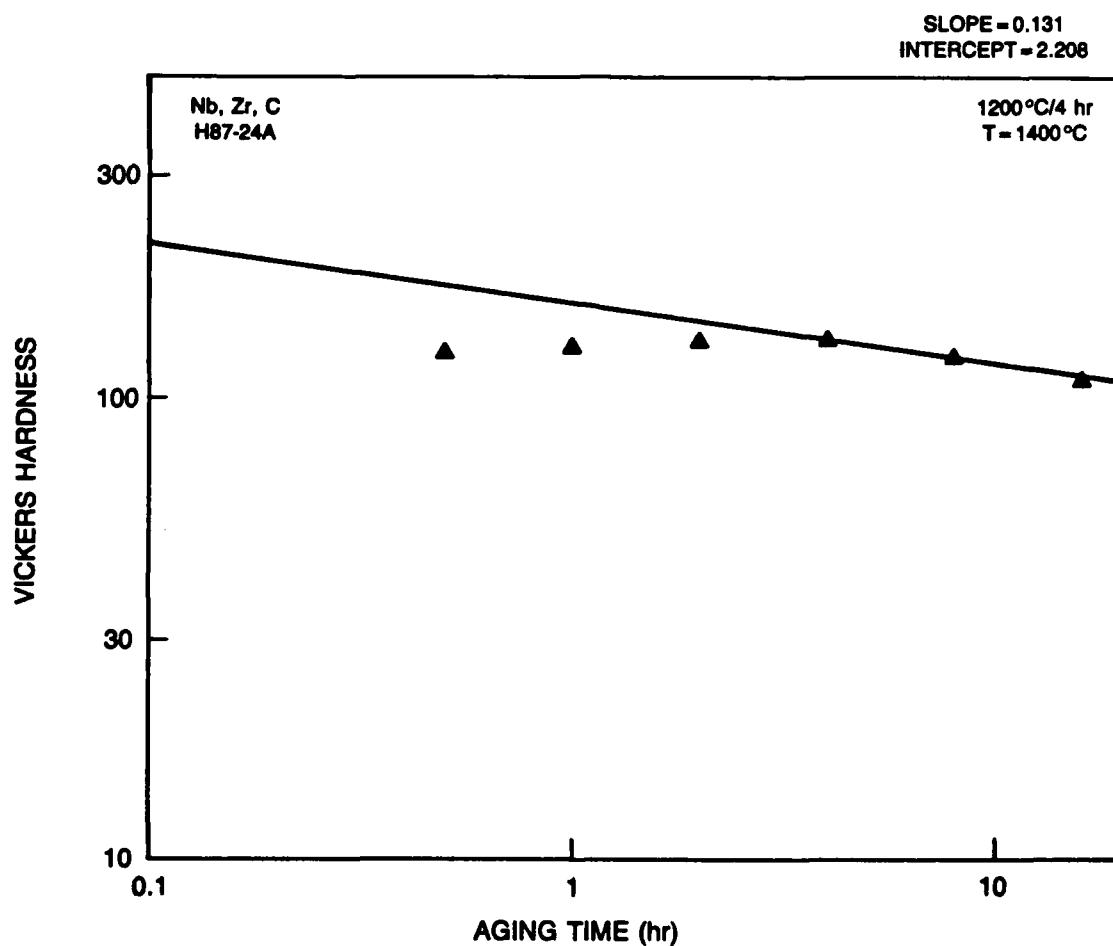
Figure 3. Isothermal Age Hardening Plot as Shown in Fig. 2 illustrating ln-ln Linear Plot in Over-Aged Region with Slope, $\Psi = 0.131$.

20 μm
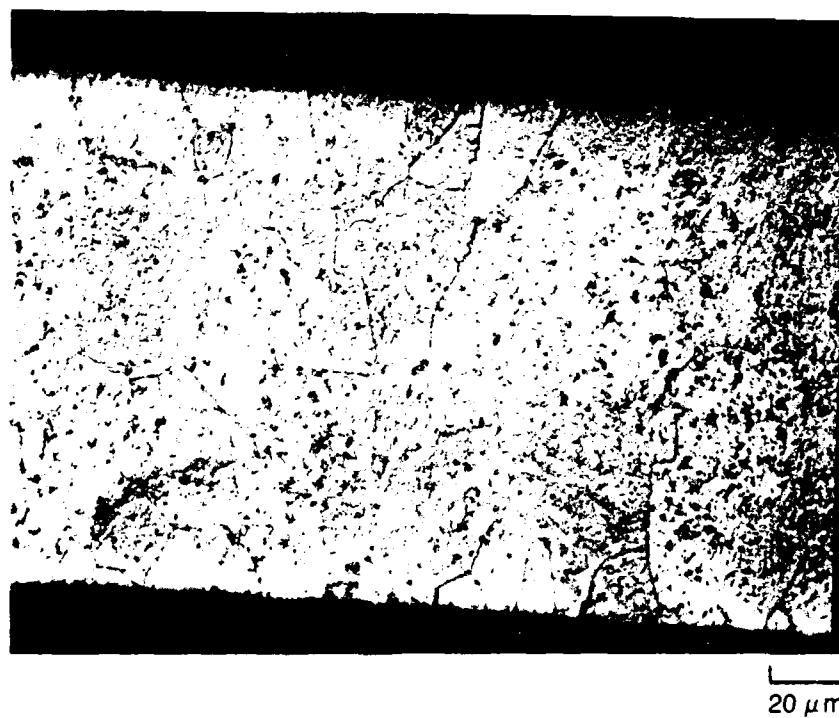
Figure 4.   Cross-Section of Zr-C Alloy Splat After Exposure at 1400°C for 8 hrs
Revealing Equiaxed Grain Structure and Fine Precipitates.

20 μm
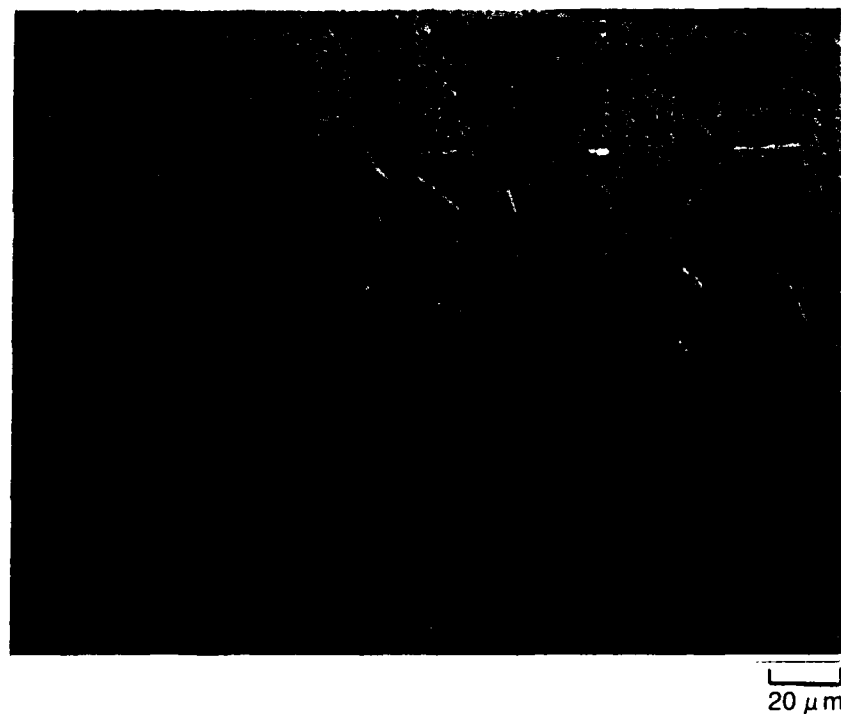
Figure 5. Cross-Section of Hf-N Alloy Splat After Exposure at 1400°C for 1 hr Revealing Equiaxed Grain Structure and Grain Boundary Precipitates.
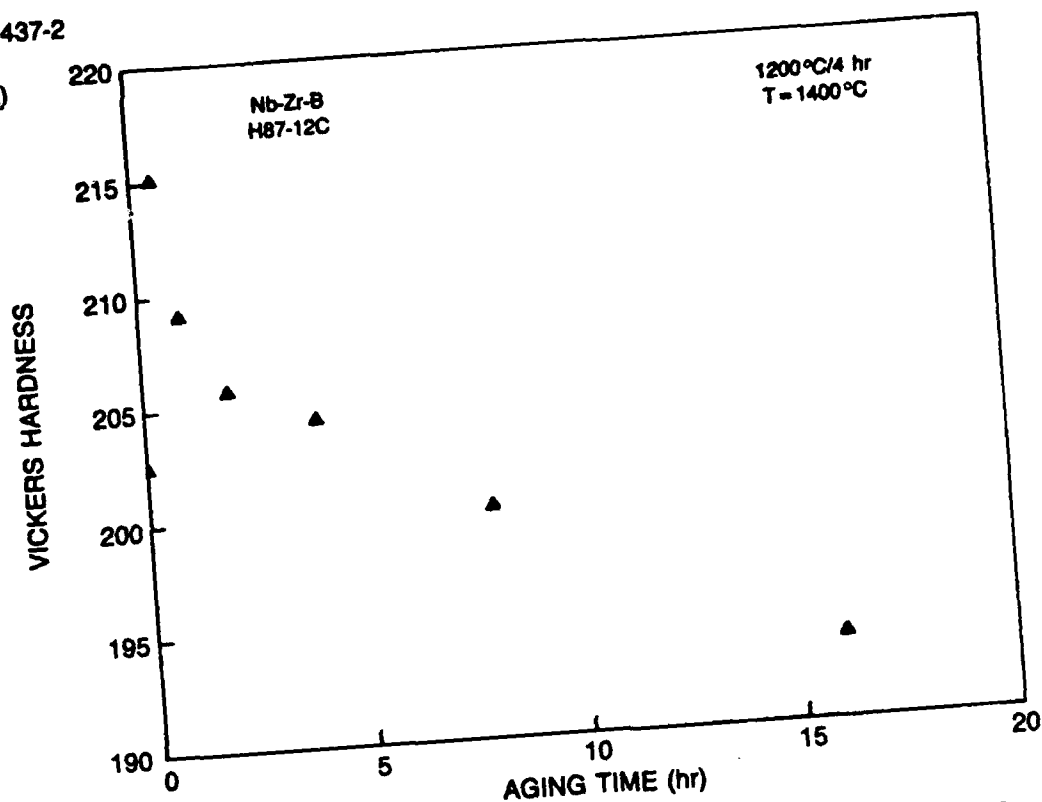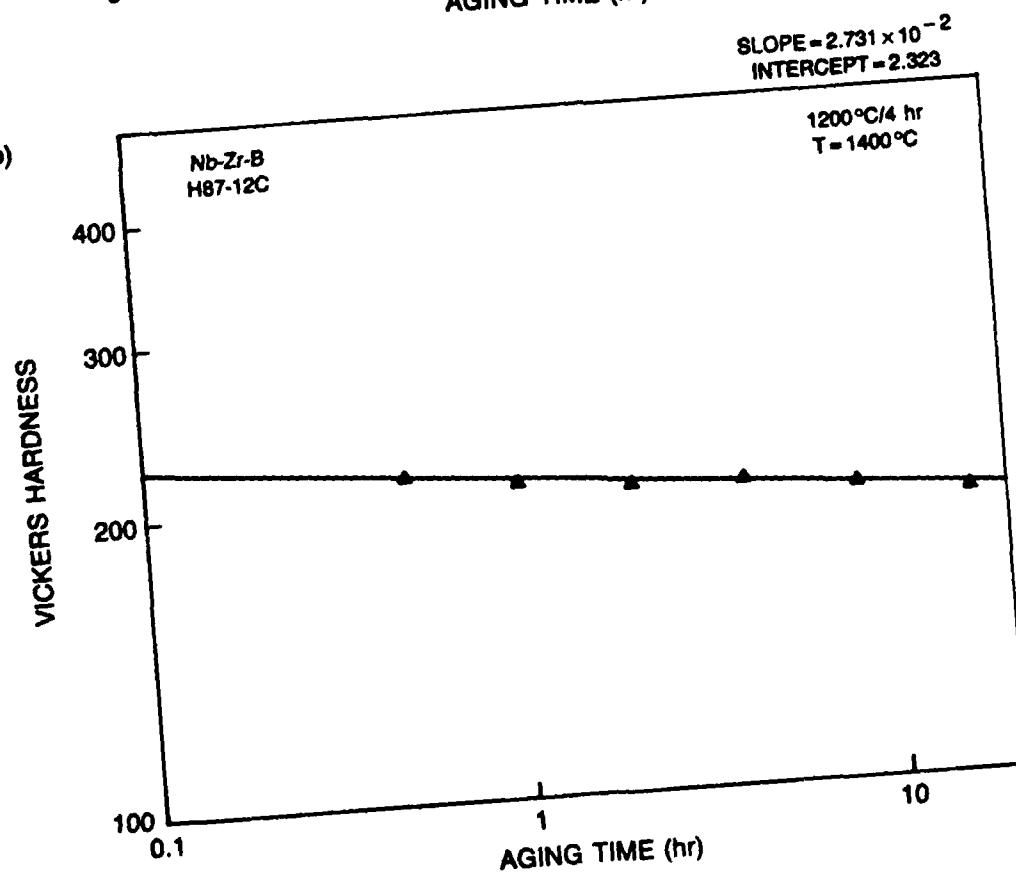
Figure 6. Isothermal Age Hardening Plots for Zr-B Alloy Illustrating (a) Rapid Hardening Followed by Over-Aging and (b) Linearized Plot Showing Excellent Fit of Data.

88—7—1—6
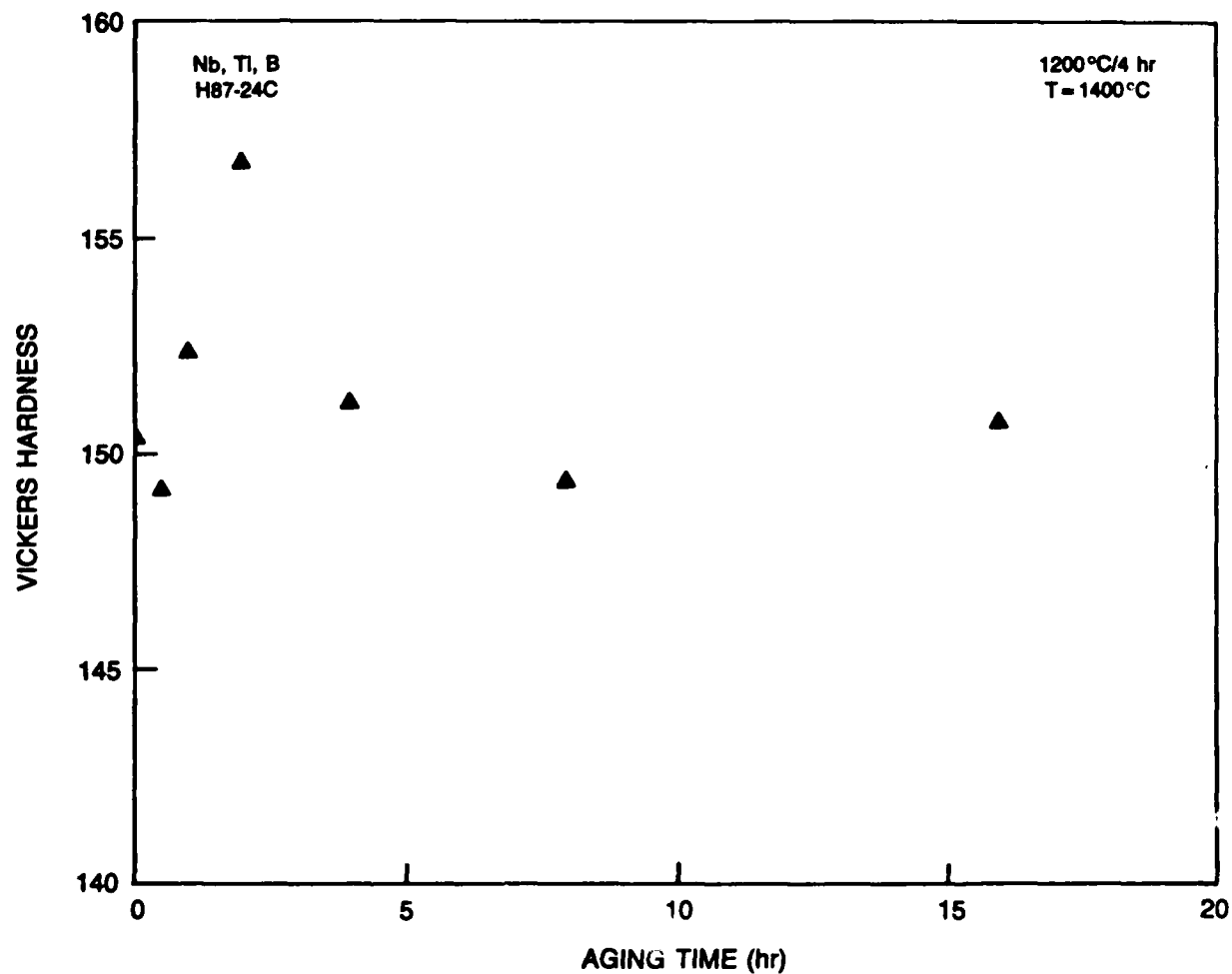
Figure 7.   Isothermal Age Hardening Plot for Ti-B Alloy Illustrating Primary and
            Secondary Hardening.
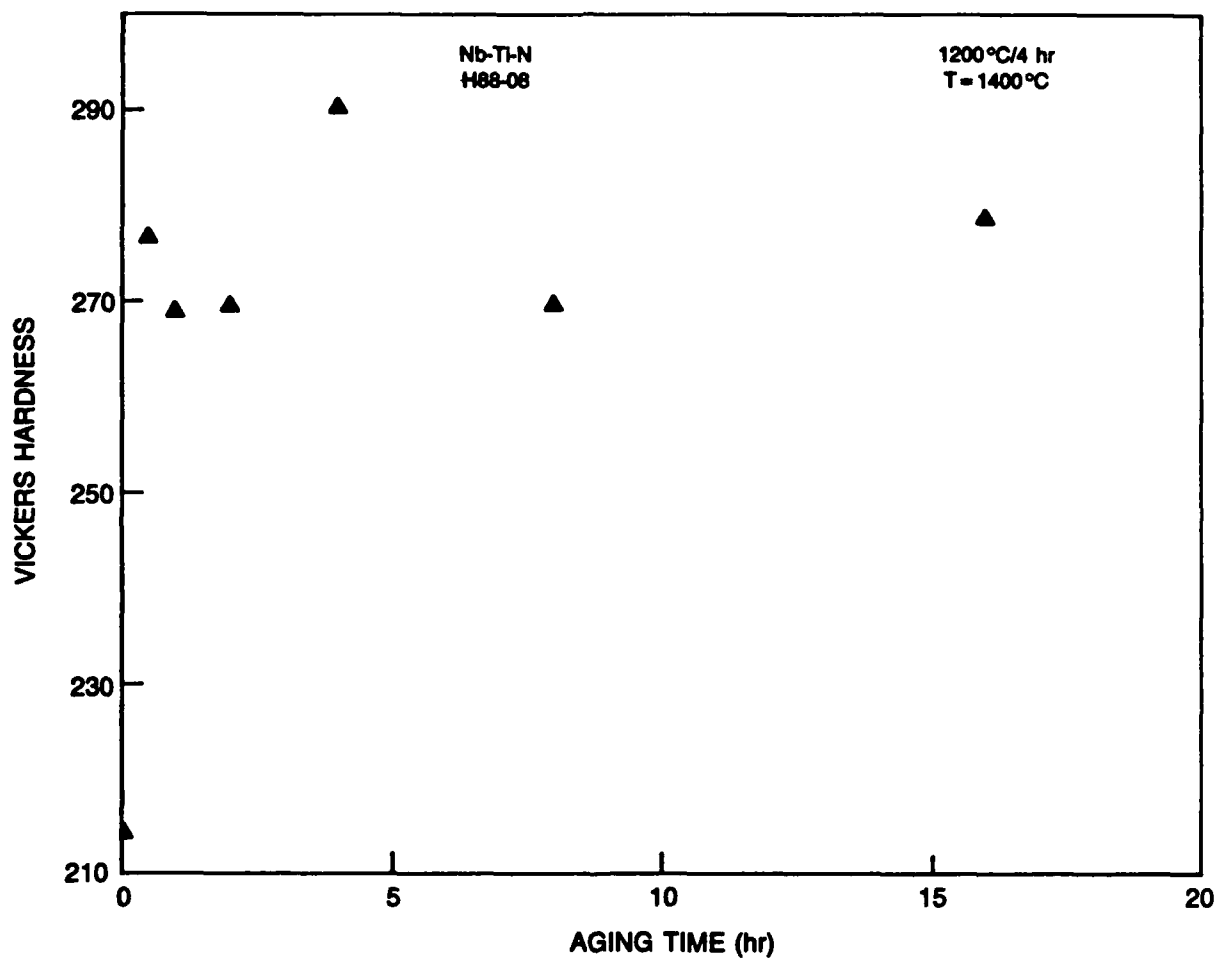
Figure 8. Isothermal Age Hardening Plot for Ti-N Alloy Illustrating Rapid Hardening on Initial Exposure to 1400°C and Negligible Subsequent Hardening.
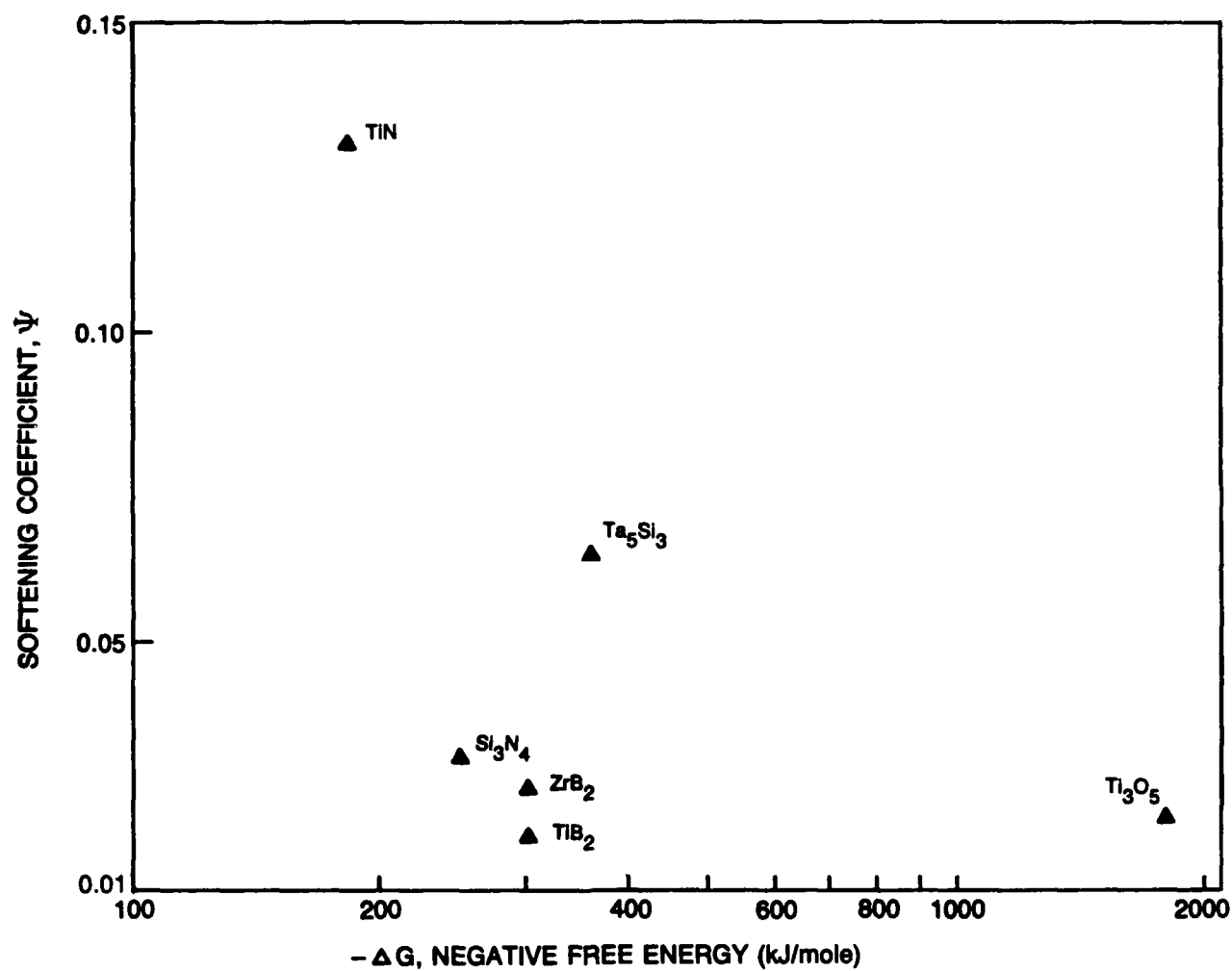
Figure 9. Plot of Ψ as a Function of $-\Delta G$ Showing a General Trend of Lower Ψ with Greater $-\Delta G$ with a Number of Exceptions Clustered in the Vicinity 200-400 kJ/mole.

1.8 μm
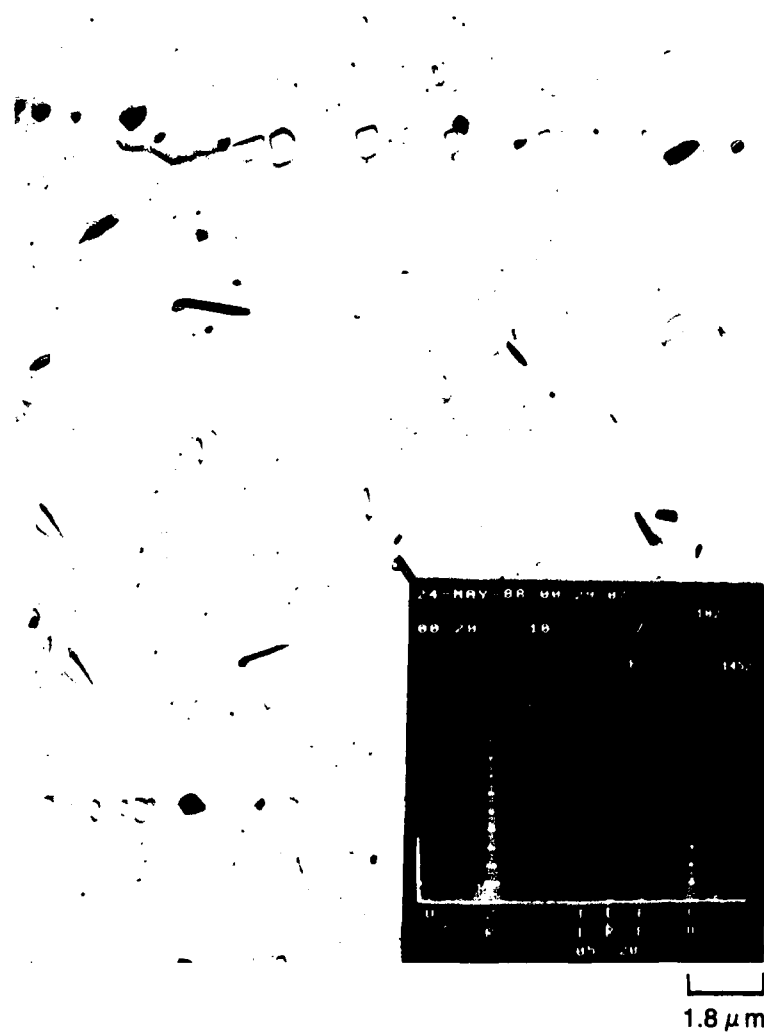
Figure 10.   Extraction Replica of Zr-B Alloy Showing Both Grain Boundary and Intra-Granular Precipitates with EDS of the Latter Inset.
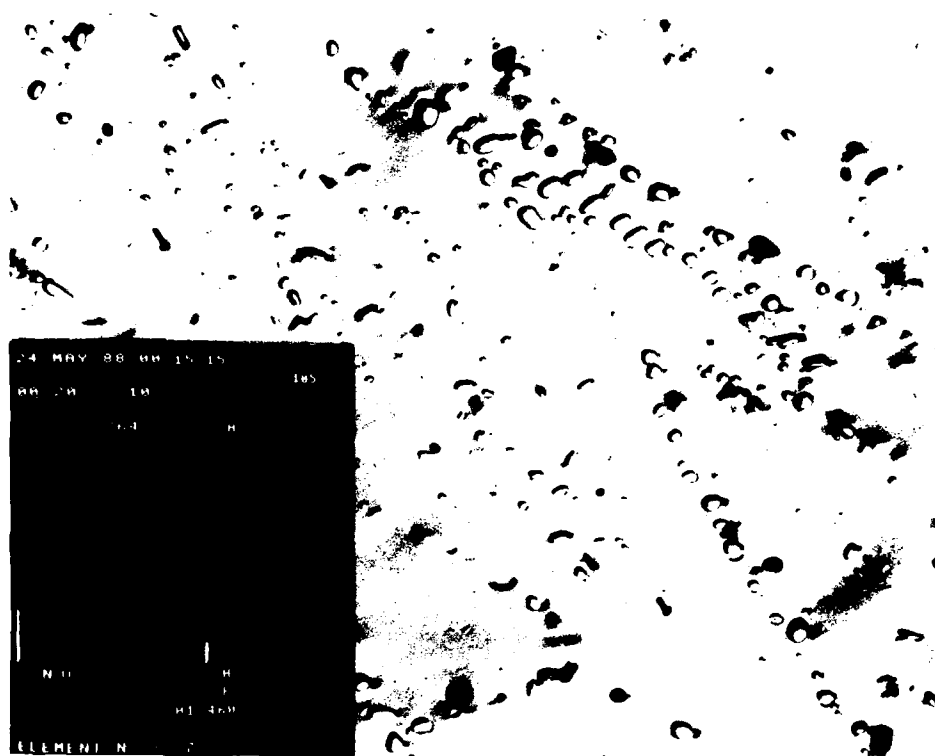
Figure 11. Extraction Replica of Hf-N Alloy Showing Both Grain Boundary and Intra-Granular Precipitates with EDS of Both Inset Showing Low Nitrogen Concentration.

1.8 µm

Figure 12.   Extraction Replica of Si-N Alloy Showing an Unidentified Plate-Like
             Precipitate and a Globular Phase.
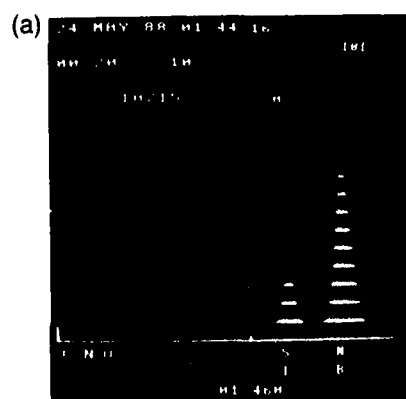
BLOCKY PHASE –ATYPICAL   BLADE PHASE
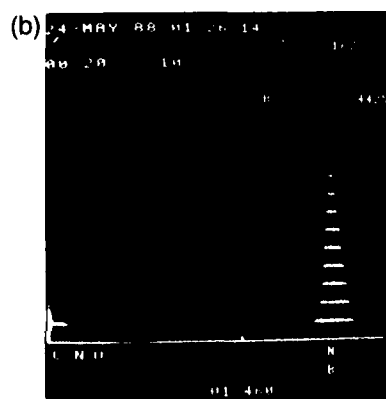
Figure 13.   EDS Analysis of Si Alloy (a) Atypical Blocky Phase of Si and Nb and (b) Plate-Like Phase with High Interstitial Element Concentration.

GENERAL VIEW OF THE MICROSTRUCTURE
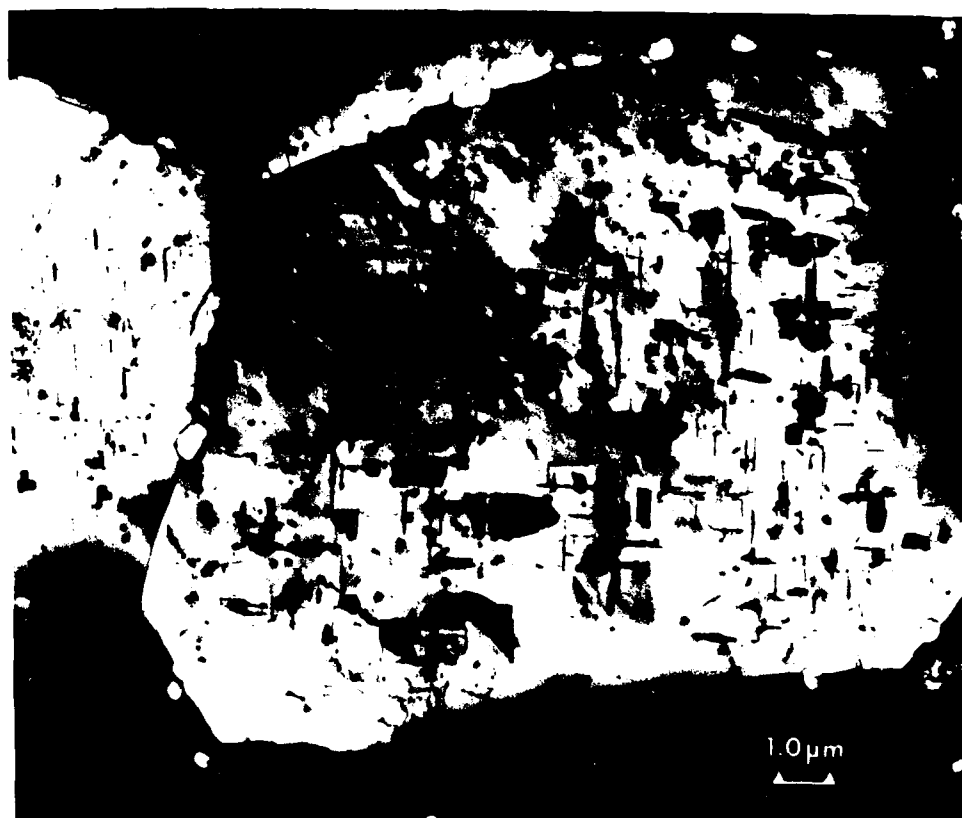
Figure 14.   Splat Quenched Nb-8Mo-0.1Ti-0.1B

(a) INTRAGRANULAR PRECIPITATES ON (100), AREA OF FIG. 14. BRIGHT FIELD,
$\bar{g}$ = PRIMARILY [002] MATRIX
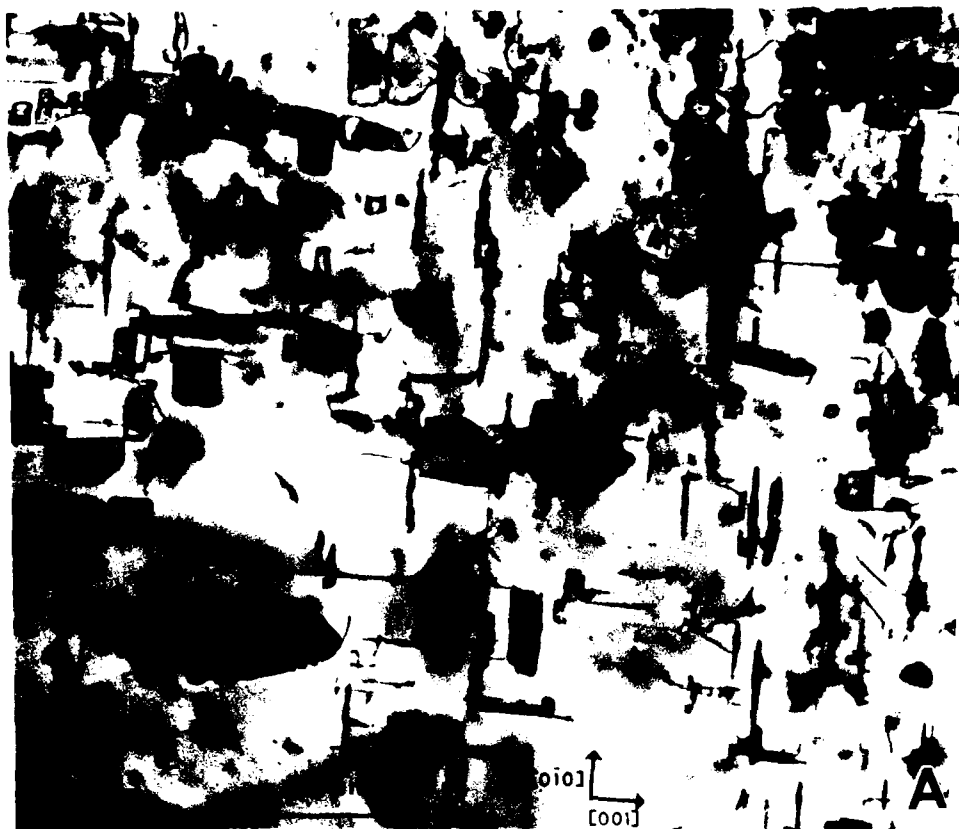
(b) SELECTED AREA DIFFRACTION PATTERN FROM CENTER OF (a), $\bar{B}$ NEAR [001]
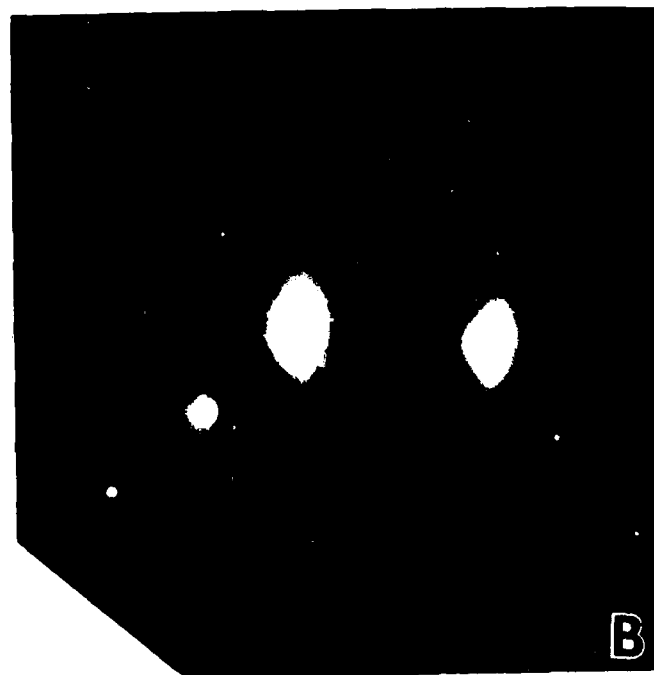
Figure 15.   Splat Quenched Nb-8Mo-0.1Ti-0.1B

88—7—1—15

(a) BRIGHT FIELD. (b) DARK FIELD, $\bar{g} = [02\bar{1}]$ NbB. (c) SADP FROM THIS AREA, $\bar{B}$ NEAR [001]. POINTER MARKS $\bar{g}$ USED FOR (b).
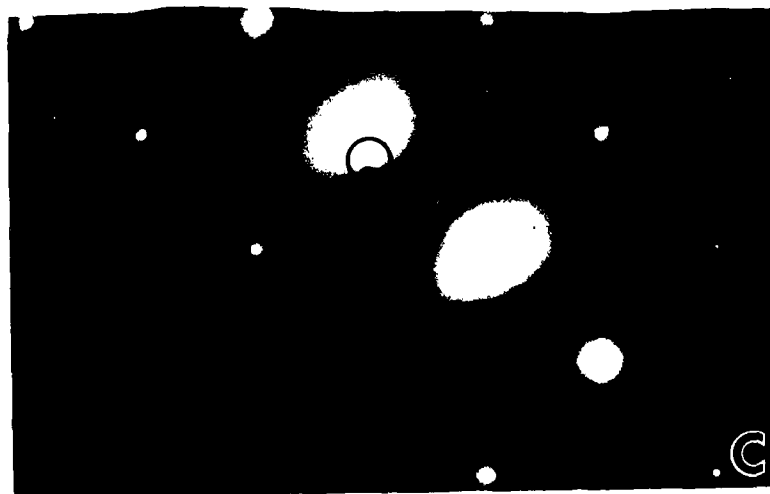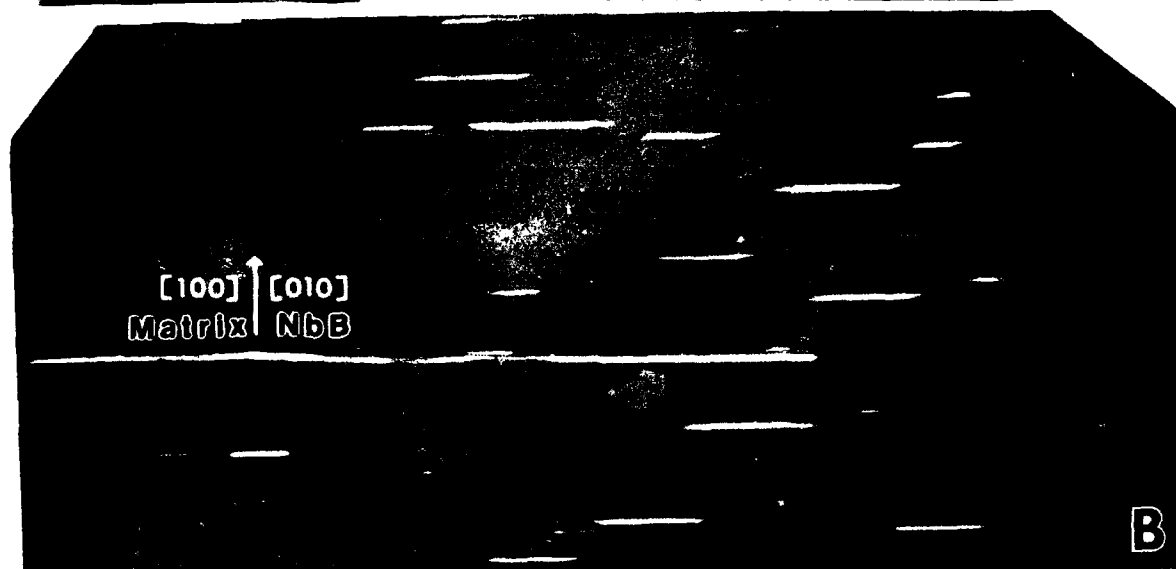
Figure 16.   Splat Quenched Nb-8Mo-0.1Ti-0.1B

**SCHEMATIC SELECTED AREA DIFFRACTION PATTERNS ILLUSTRATING THE ORIENTATION
OF ONE VARIANT OF ORTHORHOMBIC NbB TO THE BCC MATRIX (FIG. 3)**

Lattice Parameter(s): a = 3.295 Å

a = 3.292 Å   b = 8.713 Å   c = 3.165 Å
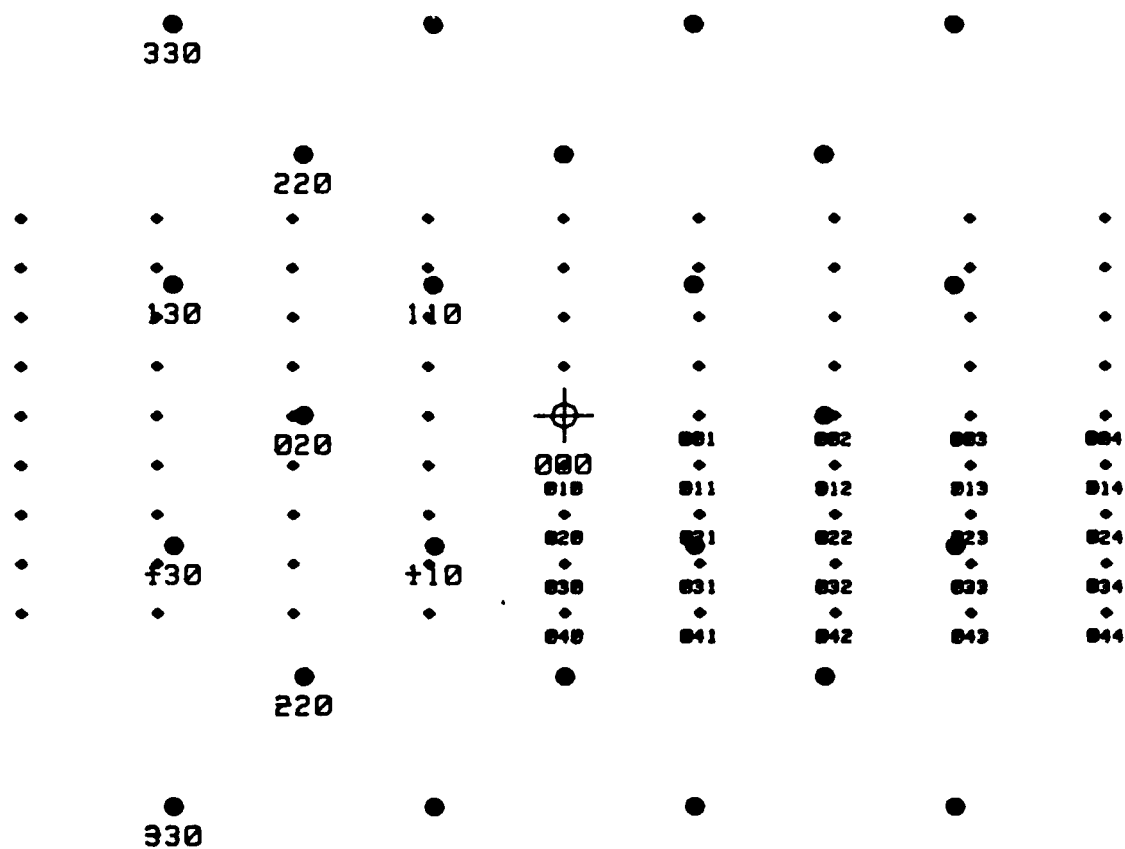
Figure 17.   Splat Quenched Nb-8Mo-0.1Ti-0.1B

GENERAL VIEW OF THE MICROSTRUCTURE

Figure 18.   Nb-1.2Ti-0.6N, Aged at 1200°C/4 hr

(a) BRIGHT FIELD. (b) DARK FIELD, $\bar{g} = [1\bar{1}01]$ Nb_2N. (c) SADP FROM THIS AREA, $\bar{B}$ NEAR [001] MATRIX AND $[11\bar{2}0]$ Nb_2N. POINTER MARKS $1\bar{1}01$ SPOT USED TO FORM (b)
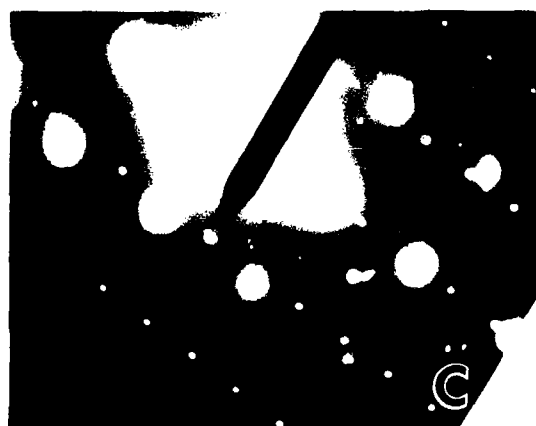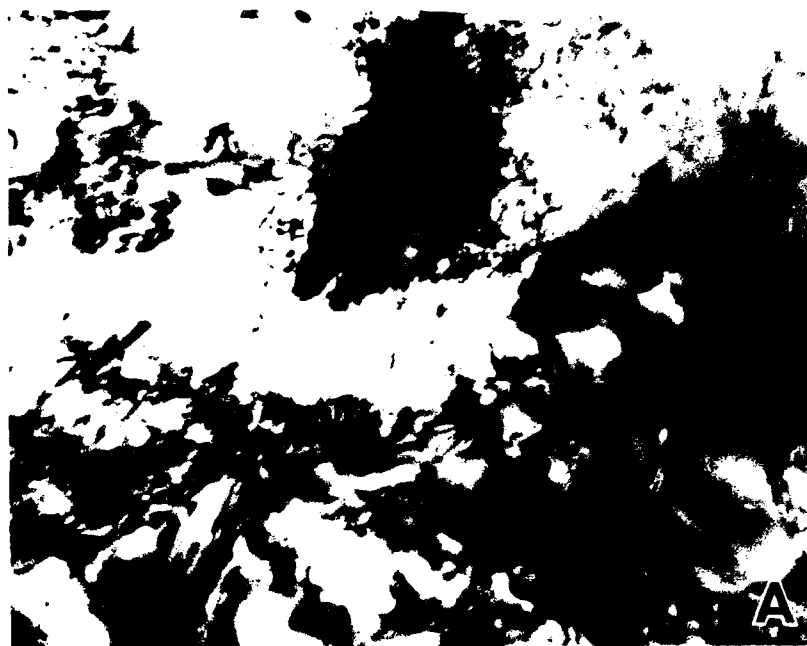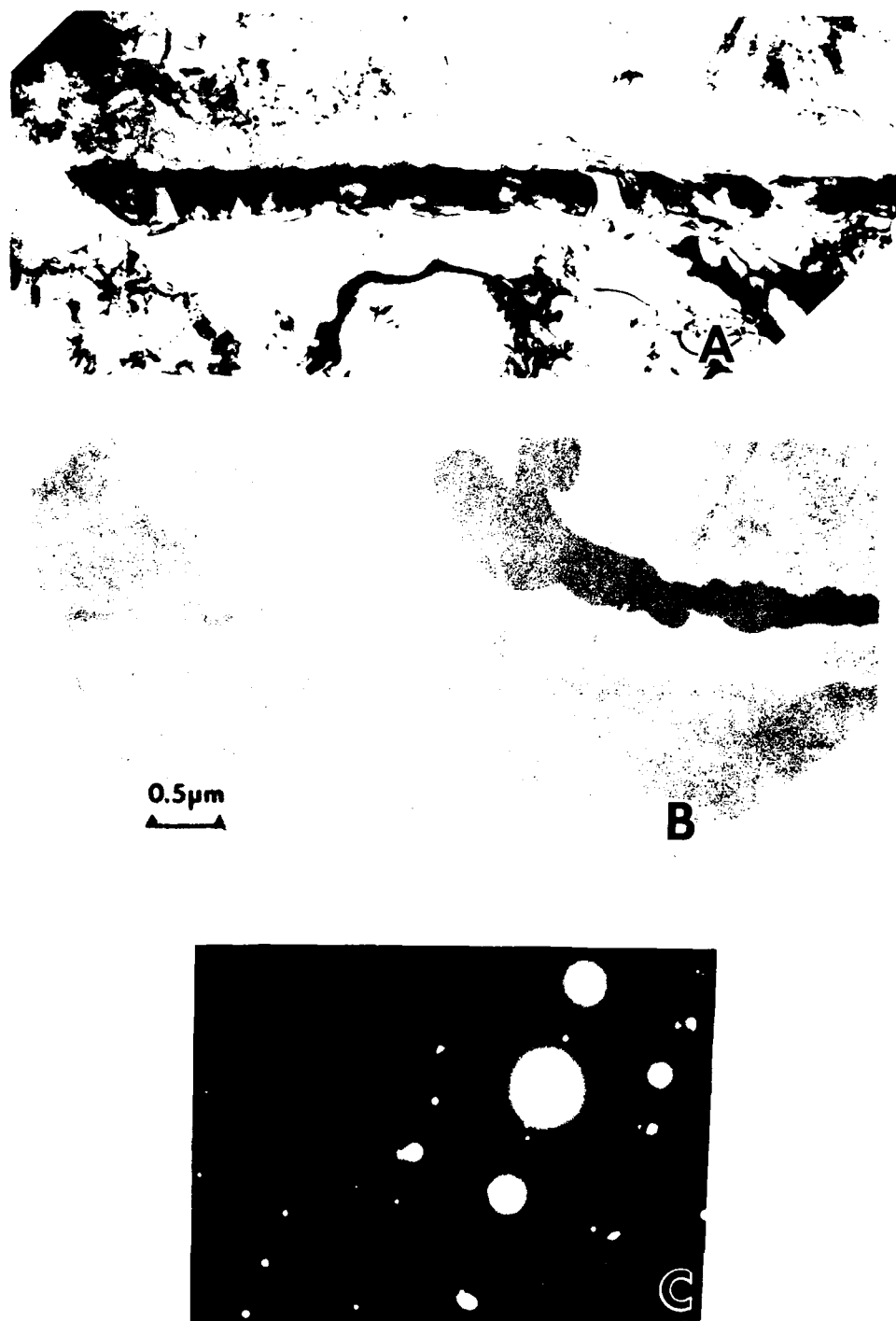
Figure 19. Grain Boundary Precipitate, Nb-1.2Ti-0.6N, Aged at 1200°C/4 hr

SCHEMATIC OF SUPERIMPOSED SELECTED AREA DIFFRACTION PATTERNS,
[001] MATRIX AND [11$\bar{2}$0] Nb$_2$N, CORRESPONDING TO FIG. 19(c)

Lattice Parameter(s):   a = 3.3007 Å
a = 3.058 Å   c = 4.961 Å
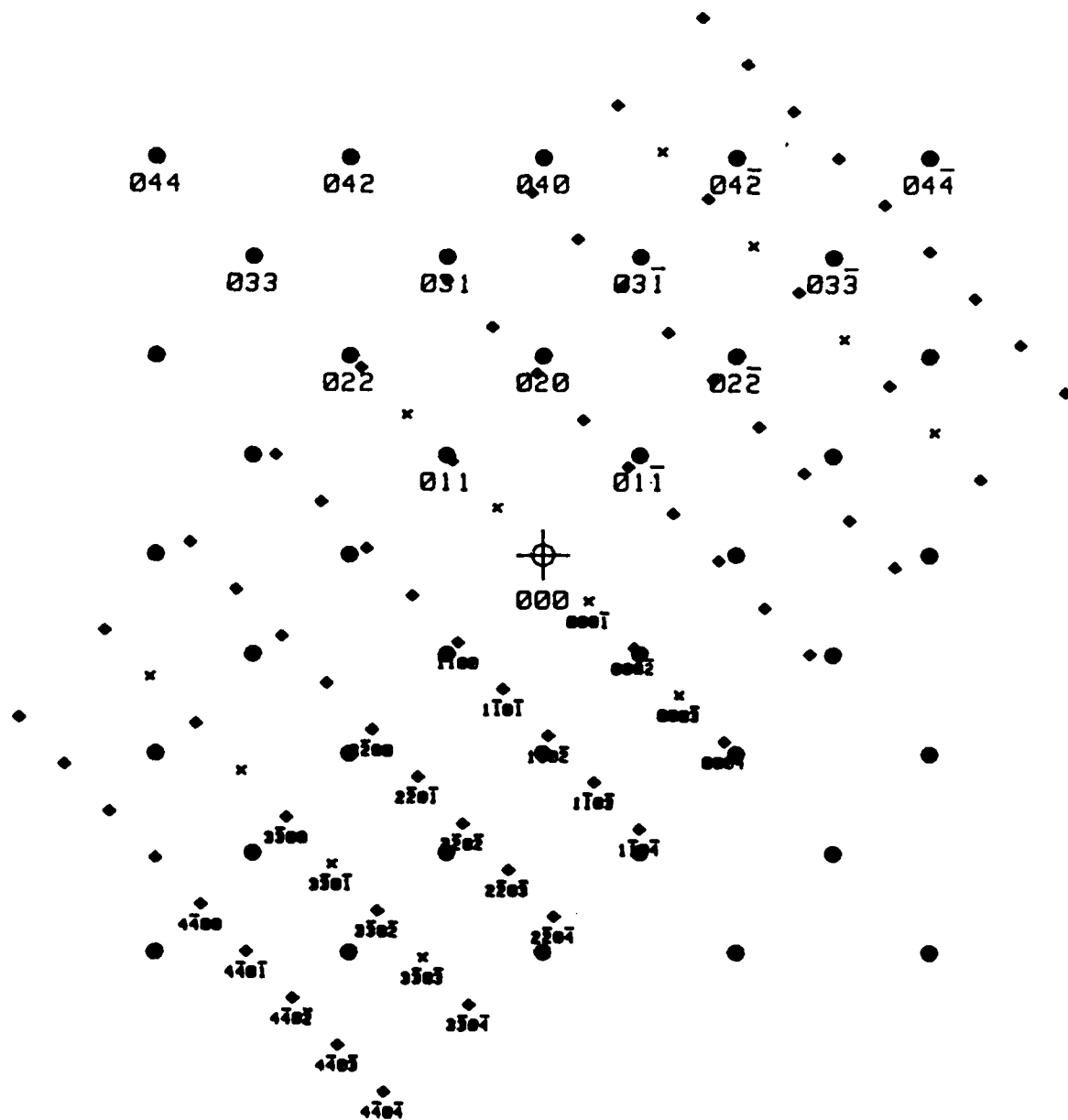
Figure 20.   Nb-1.2Ti-0.6N, Aged at 1200°C/4 hr

(a) BRIGHT FIELD. (b) DARK FIELD, $\bar{g} = [1\bar{1}02]$ Nb_2N. (c) SADP FROM THIS AREA, $\bar{B}$ NEAR [001] MATRIX AND [11$\bar{2}$0] Nb_2N. POINTER MARKS 1$\bar{1}$02 SPOT USED TO FORM (b)

0.5μm

Figure 21.   Coalesced Grain Boundary Precipitates, Nb-1.2Ti-0.6N, 1200°C/4 hr

HIGH AND LOW CAMERA LENGTH <1120> ZONE AXIS PATTERNS, PRECIPITATE
IN ROW SHOWN IN FIG. 21
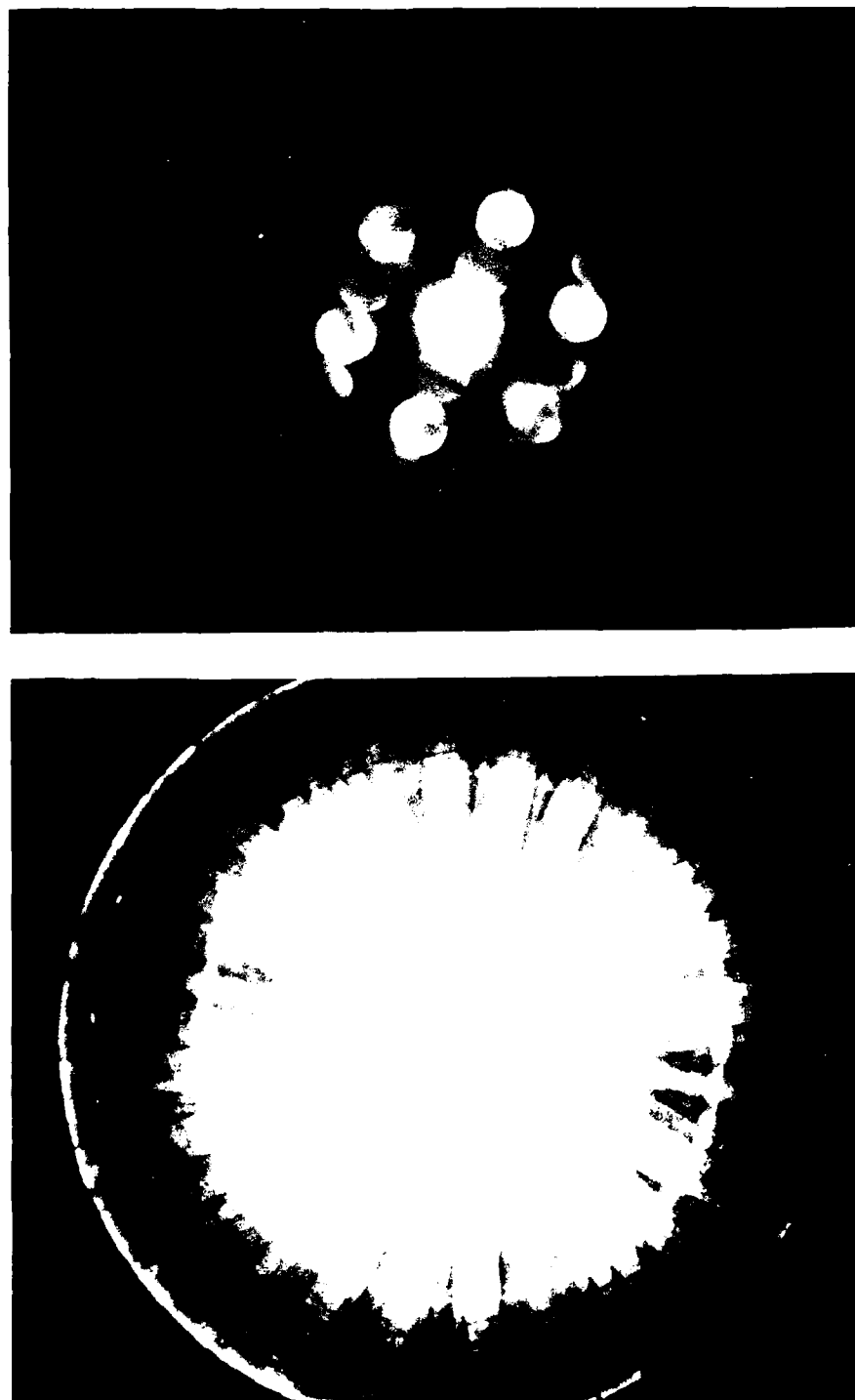
Figure 22.   CBED Patterns from Grain Boundary Precipitate, Nb-1.2Ti-0.6N, 1200°C/4 hr

(a) BRIGHT FIELD. (b) DARK FIELD, $\bar{g} = [1\bar{1}01]$ Nb_2N. (c) $[11\bar{2}0]$ SADP FROM THIS AREA, $[110]$ MATRIX PARALLEL TO $[0001]$ Nb_2N. POINTER MARKS $1\bar{1}01$ SPOT USED TO FORM (b). (d) $[11\bar{2}0]$ ZONE AXIS CONVERGENT BEAM MICRODIFFRACTION PATTERN FROM PRECIPITATE; $50\,\mu m$ CONDENSER APERTURE; 100 nm SPOT SIZE
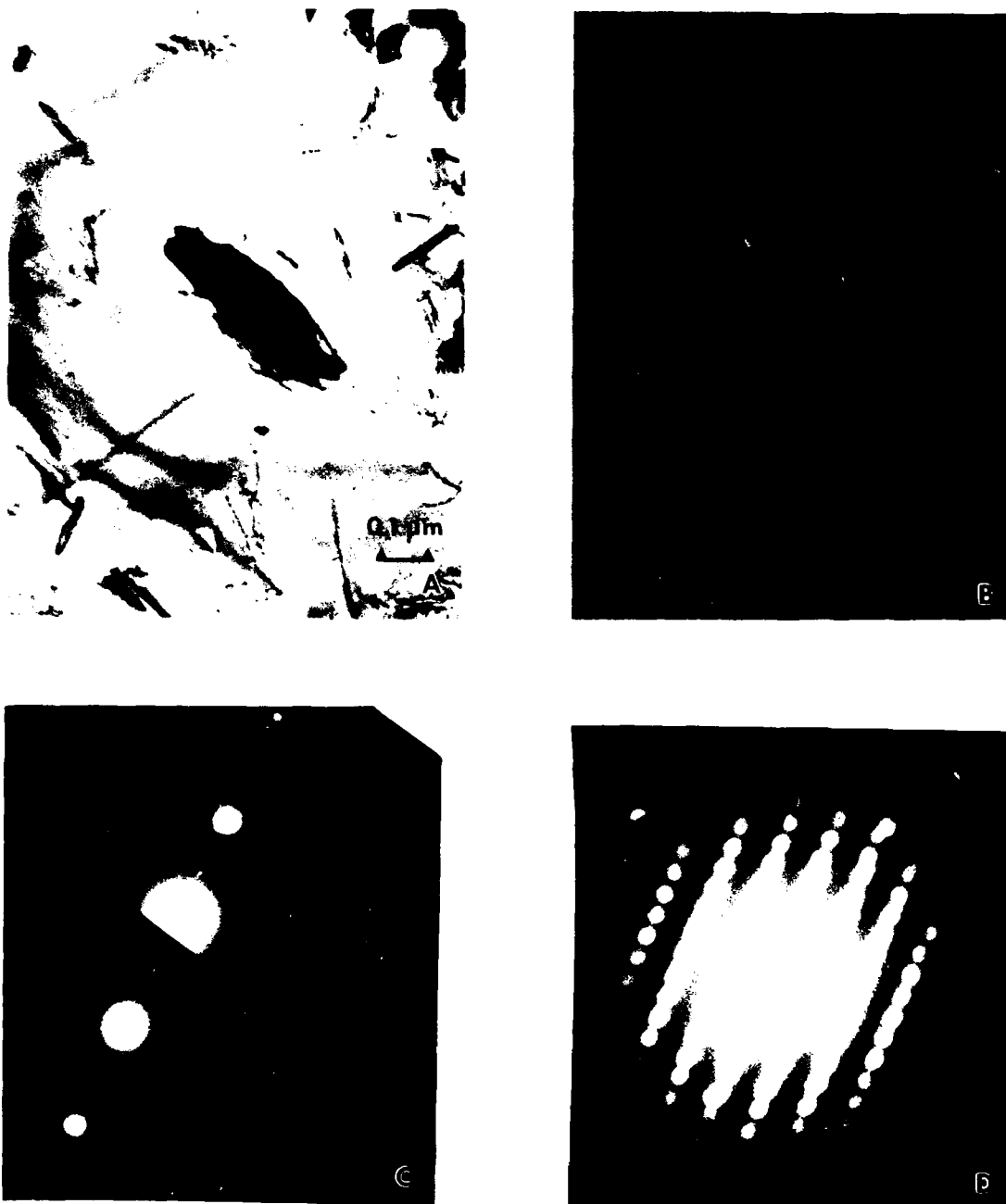
Figure 23.   Intragranular Nb_2N Precipitate, Nb-1.2Ti-0.6N, Aged at 1200°C/4 hr

(a) BRIGHT FIELD. (b) DARK FIELD, $\bar{g} = [220]$ TiN. (c) SUPERIMPOSED $[\bar{1}12]$ MATRIX AND $[\bar{1}12]$ TiN SADP'S FROM THIS AREA, ARROW MARKS 220 TiN SPOT USED FOR (b). (d) CONVERGENT BEAM MICRODIFFRACTION PATTERN CORRESPONDING TO (c), 70 μm CONDENSER APERTURE; 100 nm SPOT SIZE.

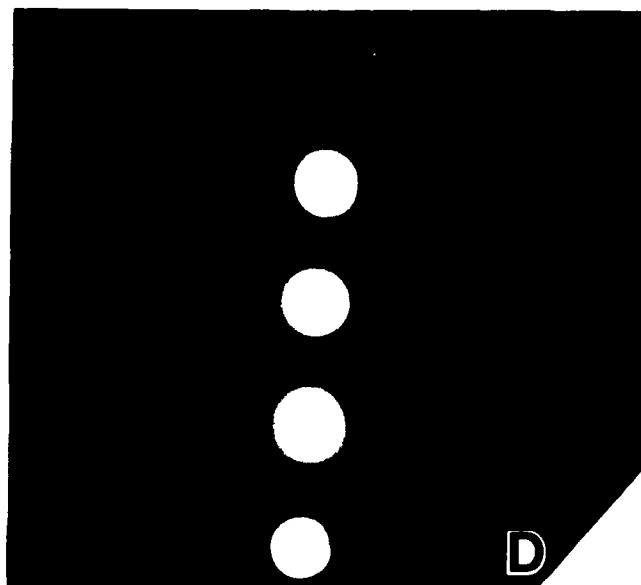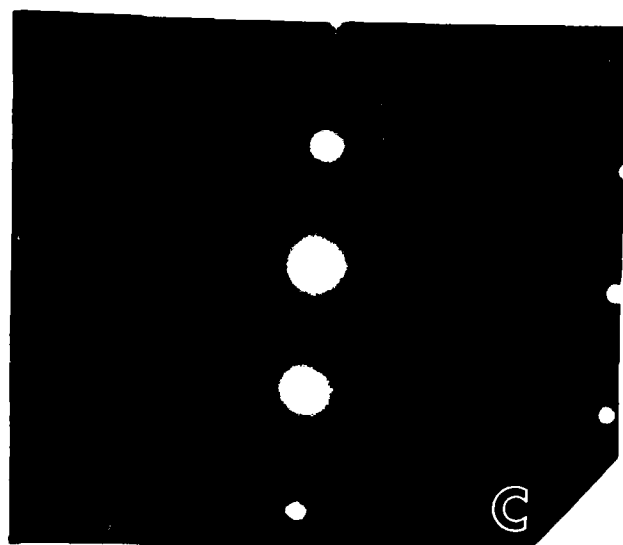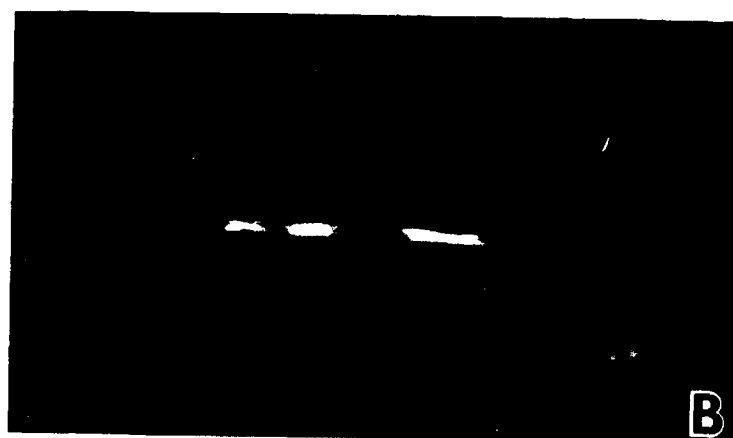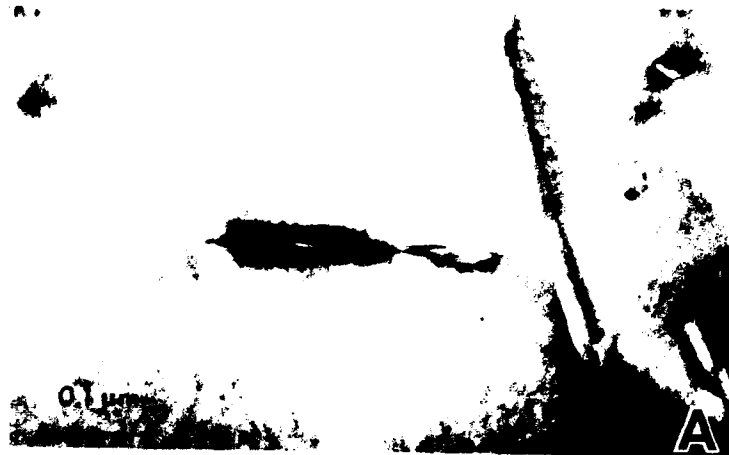**Figure 24.   Intragranular TiN Precipitate, Nb-1.2Ti-0.6N, Aged at 1200°C/4 hr**

SCHEMATIC OF SUPERIMPOSED SELECTED AREA DIFFRACTION PATTERNS, [Ī12]
MATRIX AND [Ī12] TiN, CORRESPONDING TO FIGS. 24(c) AND 24(d)

Lattice Parameter(s): a = 3.3007 Å
a = 4.224 Å

$\overline{4}\overline{4}4$

$3\overline{3}3$

$\overline{4}44$

$2\overline{2}\overline{2}$

$\overline{2}2\overline{2}$

$40\overline{2}$

$1\overline{1}\overline{1}$

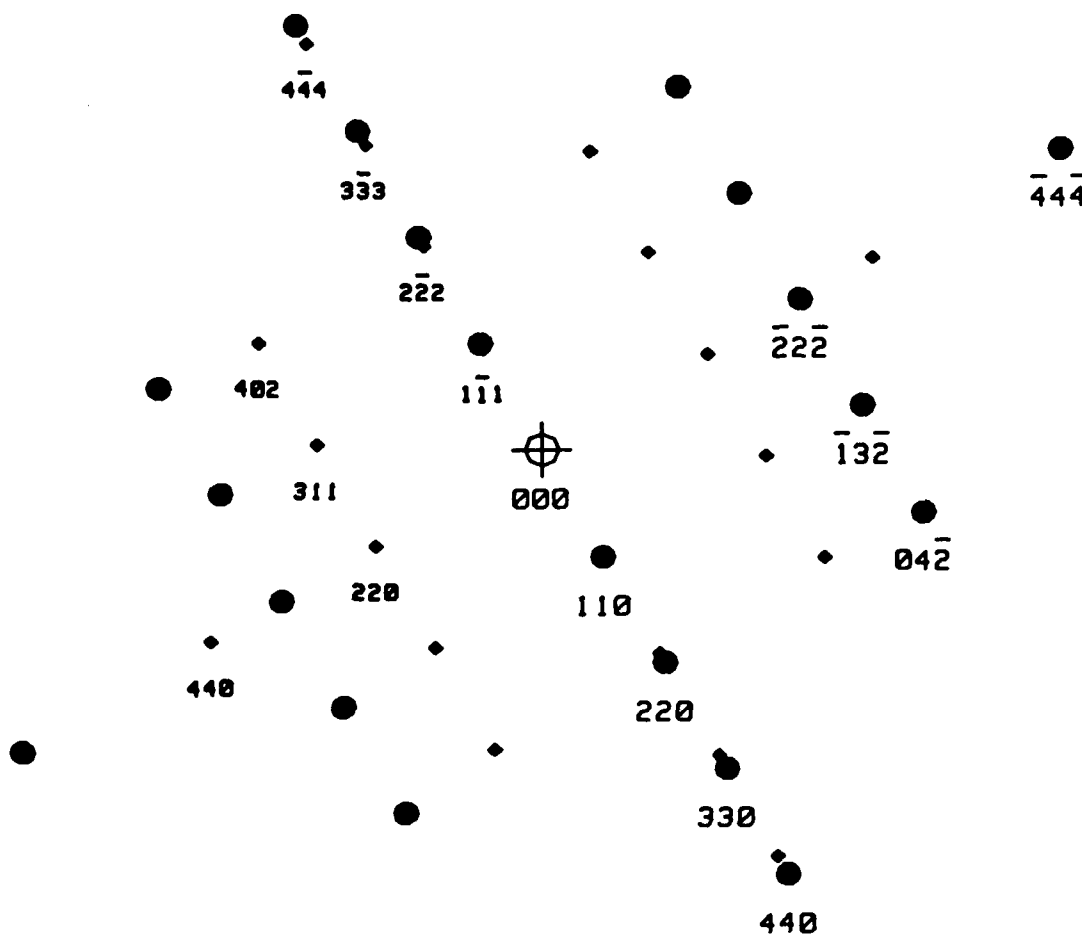$\overline{1}3\overline{2}$

311

⊕
000

$04\overline{2}$

220

110

440

220

330

440

Figure 25. Nb-1.2Ti-0.6N, Aged at 1200°C/4 hr